Report Title: Final Report for Fractionation and Separation of Polydisperse Nanoparticles into Distinct Monodisperse Fractions Using CO_2 Expanded Liquids

Type of Report: Final Scientific/Technical

Reporting Period Start Date: February 1, 2006

Reporting Period End Date: August 31, 2007

Principal Author: Christopher B. Roberts
Professor and Chair
Department of Chemical Engineering
Auburn University, AL 36849

Date Report was Issued: January 31, 2008

DOE Award Number: DE-FG26-06NT42685

Name and Address of Submitting Organization:
Christopher B. Roberts
210 Ross Hall
Department of Chemical Engineering
Auburn University, AL 36849
croberts@eng.auburn.edu

Disclaimer

Abstract

The overall objective of this project was to facilitate efficient fractionation and separation of polydisperse metal nanoparticle populations into distinct monodisperse fractions using the tunable solvent properties of gas expanded liquids. Specifically, the dispersibility of ligand-stabilized nanoparticles in an organic solution was controlled by altering the ligand-solvent interaction (solvation) by the addition of carbon dioxide (CO_2) gas as an antisolvent (thereby tailoring the bulk solvent strength) in a custom high pressure apparatus developed in our lab. This was accomplished by adjusting the CO_2 pressure over the liquid dispersion, resulting in a simple means of tuning the nanoparticle precipitation by size. Overall, this work utilized the highly tunable solvent properties of organic/CO_2 solvent mixtures to selectively size-separate dispersions of polydisperse nanoparticles (ranging from 1 to 20 nm in size) into monodisperse fractions (±1nm). Specifically, three primary tasks were performed to meet the overall objective. Task 1 involved the investigation of the effects of various operating parameters (such as temperature, pressure, ligand length and ligand type) on the efficiency of separation and fractionation of Ag nanoparticles. In addition, a thermodynamic interaction energy model was developed to predict the dispersibility of different sized nanoparticles in the gas expanded liquids at various conditions. Task 2 involved the extension of the experimental procedures identified in task 1 to the separation of other metal particles used in catalysis such as Au as well as other materials such as semiconductor particles (e.g. CdSe). Task 3 involved using the optimal conditions identified in tasks 1 and 2 to scale up the process to handle sample sizes of greater than 1 g. An experimental system was designed to allow nanoparticles of increasingly smaller sizes to be precipitated sequentially in a vertical series of high pressure vessels by moving the liquid nanoparticle dispersion from the top vessel to the bottom vessel with corresponding CO_2 pressure increases at each stage. For example, three fractions with average diameters of 7.00 nm, 4.35 nm, and 3.95 nm were recovered from a 20ml sample of Ag nanoparticles dispersed in hexane at pressures of 625 psi, 650 psi, >650 psi, respectively.

Table of Contents

Executive Summary

Fractionation and Separation of Polydisperse Nanoparticles into Distinct Monodisperse Fractions Using CO_2 Expanded Liquids

This executive summary presents a brief summary of the highlights and important accomplishments of this research project. This objective of this project was to utilize a novel, inexpensive, rapid, and efficient process for size selective fractionation of polydisperse metal nanoparticle dispersions into multiple narrow size fractions. We have developed a post-synthesis nanoparticle size-separation technique based on the tunable solvent strength of CO_2 gas expanded liquid mixtures. The dispersibility of ligand-stabilized nanoparticles in an organic solution was controlled by altering the ligand-solvent interaction through the addition of carbon dioxide (CO_2) gas as an antisolvent in a custom high pressure apparatus developed in our lab. Simply adjusting the CO_2 pressure over the liquid dispersion resulted in a straightforward means of tuning the nanoparticle precipitation by size. The highly tunable solvent properties of the organic/CO_2 solvent mixtures were used to selectively size-separate dispersions of polydisperse nanoparticles (ranging from 1 to 20 nm in size) into monodisperse fractions (±1nm).

The project objectives were achieved by using a new high pressure apparatus developed in the Roberts laboratory at Auburn University. Three primary tasks were successfully achieved including: 1) Investigation of the effects of various operating parameters (such as temperature, pressure, ligand length, and ligand type) on the efficiency of separation and fractionation of Ag nanoparticles. 2) Extend the experimental procedures identified in task 1 to the separation of other metal particles used in catalysis such as Au as well as other materials such as semiconductor particles (e.g. CdSe). 3) Use the optimal conditions identified in tasks 1 and 2 to scale up the process to handle lager sample sizes (e.g. >20 ml metal nanoparticle dispersions).

Polydisperse liquid dispersions of metal (Ag, Au) nanoparticles capped with alkane (e.g. dodecane thiol) ligands and semiconductor (CdSe/ZnS) nanoparticles capped with TOPO ligands were successfully separated and fractionated into very monodisperse size fractions (± 1 nm) using the adjustable solvent strength of CO_2 gas expanded alkane solvent mixtures by simply adjusting the applied CO_2 pressure. We have shown that an expansion of the organic solution occurs upon increasing pressurization with CO_2 gas due to the miscibility of CO_2 with the organic solvent and the addition of CO_2 to the organic solution thereby acts as an antisolvent for the non-polar ligands. This has allowed the size selective precipitation of the nanoparticles from the expanded liquids with simple adjustments in CO_2 pressure. We have found that particle dispersability in a solvent mixture requires a sufficient solvent-ligand interaction in order to provide enough repulsive force to overcome the van der Waals forces of attraction between the particles in solution. Hence, the degree of solvent-ligand interaction is diminished upon the gradual addition of CO_2 antisolvent through pressurization and since the larger particles in solution have greater van der Waals forces of attraction, the larger particles begin precipitation first upon worsening solvent conditions. CO_2 gas was chosen as the antisolvent in this case because it is a feeble solvent with zero dipole moment and a low dielectric constant. Moreover, the physico-chemical properties of CO_2 gas expanded liquids can be finely tuned with simple adjustments in temperature and pressure. These systems allow the solvent-ligand interactions, and hence nanoparticle dispersability to be finely tuned with adjustments in CO_2 pressure. Detailed studies were performed to understand the influence of various factors on the size separation process, such as the types of metal nanoparticles (Ag, Au), ligand type, solvent type, temperature, pressure, recursive fractionation stages and the effect of holding time. In all, we have found that this process is extremely reproducible since particle precipitation is precisely controlled by exact manipulations of solvent strength through adjustments in the CO_2 pressure. In addition, we have successfully performed the size

separation of TOPO capped semiconductor (CdSe/ZnS) quantum dots using this technique. We have also developed a thermodynamic model to predict the conditions under which these separations are viable and to determine the sensitivity of the separation process to certain process variables. We have also successfully scaled up this gas expanded liquid nanoparticle separation process for nanoparticle dispersions of greater than 20ml. Specifically, an experimental system was designed to allow nanoparticles of increasingly smaller sizes to be precipitated sequentially in a vertical series of high pressure vessels. In this case, the the liquid nanoparticle dispersion is moved by gravity from the top vessel to the bottom vessel with corresponding CO_2 pressure increases at each stage. As an example, 20 ml of a hexane dispersion of dodecane thiol capped Ag nanoparticles with average diameter 5.59 nm and 50.7% relative standard deviation was successfully separated into three distinct fractions with average diameters (and relative standard deviations) of 7.00 nm (41%), 4.35 (21.7%), and 3.95 (27.7%). These fractions were collected using CO_2 pressures of 625 psi, 650 psi, >650 psi, respectively. While this larger volume separation is not as effective as the smaller volume separations, we have shown that this apparatus and method is capable of separating a very polydisperse original dispersion into distinct, narrow size fractions.

Report Details

The remainder of this report provides specific details about the various aspects of both the experimental (small and larger scale nanoparticle size fractionations) and the thermodynamic modeling of the separation process.

Many nanoscale materials manifest unusual mechanical, chemical, magnetic, and optical properties which can be utilized in applications demanding improved or specialized performance. Not only do these properties arise on the nanoscale, but they are also often size dependent. Thus, controlling the size and size distribution can provide opportunities to tune the special characteristics of nanomaterials for chosen applications. Spherical nanoparticles in particular have received considerable attention since they allow for an investigation of basic properties of nanomaterials. However, despite the widespread interest and investigation of ligand stabilized nanoparticles over the last decade, relatively little improvement has been made to the time consuming and solvent intensive techniques employed for isolating monodisperse particle populations of ligand stabilized particles. We have developed a greatly improved method for obtaining monodisperse particle populations from an initially polydisperse solution of ligand capped metal nanoparticles.[1]

The size dependent properties of nanoscale materials allows them to be engineered to have specific functions such as in catalysts, quantum dots for optical properties, size dependent conduction of electrons in Ag nanoparticles and in the production of high quality ordered arrays and ordered thin films. While solution based nanoparticle formation techniques are attractive due to their simplicity, they often result in synthesis of particles with a wide size range (e.g. 1 to 20 nm). As such, post synthesis processing is required to further refine the size distribution to the desired monodisperse range. A variety of post-synthesis techniques have been developed to narrow size distributions including the use of liquid antisolvents to selectively control precipitation, isoelectric focusing electrophoresis (IEF)[2] and chromatography techniques. Addition of liquid antisolvent such as ethanol is the most commonly used method to cause size selective nanoparticle precipitation from organic solution. But in addition to being time consuming and solvent intensive, the technique can be subjective as it is often based on the observed opalescence of the solution upon antisolvent addition. This report presents a process for rapid and precise size separation of polydisperse nanoparticle populations into mondisperse fractions using the pressure tunable physico-chemical properties of CO_2 gas expanded liquid (GEL) solutions where CO_2 acts as an antisolvent.[3] To improve our fundamental understanding and to further refine the size separation process, this study is being performed to identify the key parameters enabling size separation of various nanoparticle populations.

Process Development for Size Selective Precipitation of Silver and Gold Nanoparticles

Materials for Metal Nanoparticles. Silver nitrate (99.8% purity)($AgNO_3$) was obtained from Acros. Hydrogen tetrachloroaurate trihydrate (99.9%) ($HAuCl_4.3H_2O$), tetraoctylammonium bromide (98%), chloroform (99.8%), sodium borohydride (99%), dodecanethiol (98%), hexanethiol (95%), octanethiol (98.5%), tetradecanethiol (98%), hexane (99%), cyclohexane (99.5%), octane (99%) and heptane (99%) were obtained from Aldrich chemical Co. Pentane (99.6%), toluene (99%) and deionized water (D-H_2O) was obtained from Fisher. Ethanol (200

proof) was obtained from Florida Distillers. Carbon dioxide (SFC/SFE grade) was obtained from Airgas. All chemicals were used as supplied.

Metal Nanoparticle Synthesis. Ligand stabilized silver and gold nanoparticles were synthesized by the two phase arrested precipitation method as developed by Brust et. al. [4]
In short, a solution of 0.19g of $AgNO_3$ in 36 mL of D-H_2O was mixed with an organic solution of 2.7 g of tetraoctylammonium bromide in 24.5 mL of chloroform. The mixture was stirred for 1 hr, the aqueous phase was removed, and then 240μL of dodecanethiol were added. A solution of 0.5 g of $NaBH_4$ in 30 mL of D-H_2O was added as a reducing agent after stirring the mixture for 5-10 min. The mixture was stirred for 4-12 h before discarding the aqueous phase. In addition to dodecanethiol, other thiols were used to examine the effect of thiol length on the size separation process. In each case, the mole percentage of thiol added was the same as that of the dodecanethiol described above. Gold nanoparticles were synthesized by replacing 0.19g of AgNO3 with 0.38g of hydrogen tetrachloroaurate trihydrate ($HAuCl_4 \cdot 3H_2O$), replacing chloroform with toluene, and adding thiol after 4-12 hours of stirring. The delayed addition of thiol was performed to accommodate the higher affinity of the ligands to gold particles.
Once the thiol coated metal particle dispersion was formed, ethanol was added as antisolvent. The dispersion of nanoparticles in the solvent/antisolvent mixture was then centrifuged (Fisher Centrific Model 228) to precipitate out the metallic nanoparticles. The particles were again washed with ethanol and centrifuged to remove any unbound ligands. This process of washing with ethanol was repeated 3 times to remove the phase transfer catalyst. The particles were then dispersed in hexane by sonication (Fisher). The remaining dispersion of nanoparticles in hexane was used for further experimentation.

UV-visible Absorbance Spectroscopy. The UV–visible absorbance spectrum of the particle dispersions in both neat solvent and in the CO_2 expanded solvents was measured in a high pressure view cell with a Varian 300E spectrophotometer to monitor the precipitation of gold particles with added CO_2 pressure. The cell had a stainless steel body with two O-ring sealed windows on opposite ends. The optical path length of the cell was 3 cm. A quartz cuvette of 10mm path length was filled with 3mL of organic solvent and 200μL of the hexane solution of dispersed nanoparticles. A Teflon cuvette holder was then used to position the dispersion in a quartz cuvette at the centerline of the windows. The view cell was then pressurized with CO_2 using an ISCO 260D syringe pump and UV-Vis absorbance spectra were collected at each operating pressure until the maximum absorbance value reached a steady value. This was an indication of an equilibrium condition being reached in terms of particle dispersion.

Size Selective Precipitation Process. The spiral tube apparatus as shown in Figure 1 was fabricated to obtain monodisperse metal nanoparticle populations[3] from an initially polydisperse population through precipitation at specific locations on a surface via CO_2 pressurization. This apparatus involves a 12 cm long, 2 cm diameter glass tube modified to include a concentric, spiral indentation on the surface of the tube from one end to the other. These indentations provide a 6mm deep, 2.5 cm wide spiral channel, or groove, inside of the tube that allows a liquid droplet of nanoparticle dispersion resting within the channel to be translated from one location to another by a simple rotation of the tube while keeping the length of the tube horizontal.

The spiral tube is situated within a cylindrical high pressure stainless steel view cell equipped on one end with an O-ring sealed quartz window for observation. The other end is fitted with Teflon tapered high pressure fitting that allows entry of a 1/8 in. stainless steel rod attached to the spiral tube with a Teflon interconnect. This assembly allows radial rotation of the spiral tube within the high pressure vessel by simply turning the metal rod from outside the vessel while a dynamic high pressure seal is maintained by the Teflon fitting. The location of a liquid droplet situated in the glass tube channel (inside the tube) can then be controlled by turning the steel rod.

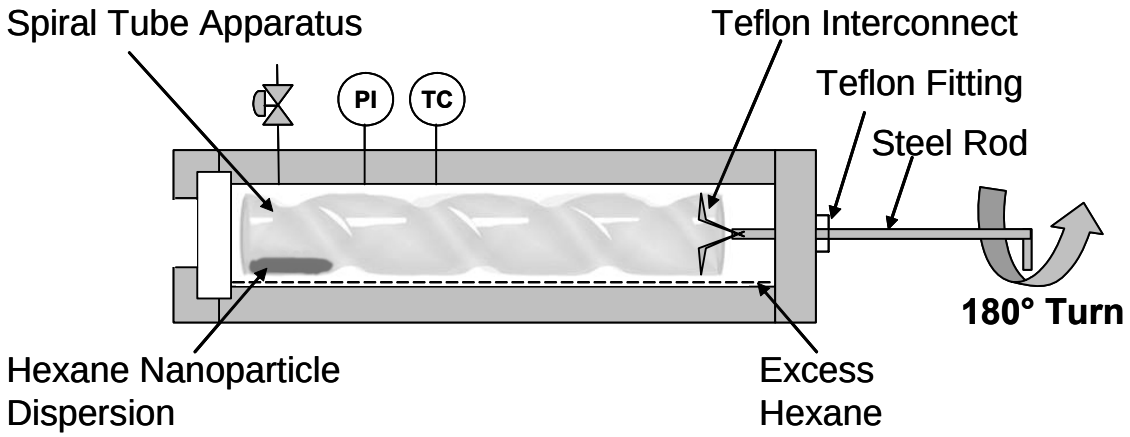

Figure 1. Nanoparticle size selection apparatus enclosed in a high pressure vessel shows loading of hexane nanoparticle dispersion. Excess hexane was loaded for saturating the high pressure vessel with hexane vapor. Teflon fitting allows the steel rod to enter into the vessel and maintains the high pressure seal while turning the steel rod 180^{o} which rotates the spiral tube with the help of Teflon interconnect. PI and TC stand for pressure indicator and temperature controller respectively.

The process was initiated by introducing 700μL of pure hexane into the high pressure view cell in the annular space outside of the spiral tube and allowing it to sit for at least 10 min. This hexane was introduced to saturate the system with hexane vapor prior to introducing the nanoparticle dispersion sample. This was done in order to minimize evaporative losses of hexane from the dispersion droplet during the separation process. Next, 250μL of the hexane dispersion of thiol coated metal particles was introduced into the channel of the spiral tube at the horizontal position closest to the quartz window as shown in the top image in Figure 2. The vessel was then slowly pressurized to an initial pressure of 550 psi and allowed 20 min to equilibrate at location A in the spiral tube. Of the overall 950μL of hexane introduced into the 60 ml vessel (both inside and outside of the spiral tube), 15% of this hexane is dissolved into the CO_2 gaseous phase at equilibrium at 500psi and 25^{o}C, and this partitioning is increased to 22% of this hexane dissolved into the CO_2 at the highest pressure of 700psi as determined by phase equilibrium calculations using the Peng Robinson equation of state. More importantly, the increased concentration of CO_2 in the solvent mixture (liquid phase) decreases the overall solvent strength such that particles too large to be stabilized by the now weakened CO_2/solvent mixture will precipitate during this 20 minute settling time.

Van der Waal's forces cause the particles to adhere to the surface on which they precipitate. To separate the remaining liquid dispersion from the precipitated particles, the tube was rotated by turning the rod 180°. This rotation moves the liquid dispersion to the next location B (180° around the tube, but further along axially) leaving behind the precipitated particles affixed to the spiral groove A. The vessel was then pressurized to 600 psi with the suspension at the new location; the particles that precipitate at this pressure are, on average, smaller than those that precipitated at the lower pressure. The glass tube is then turned another 180° to take the dispersion to a new location C leaving this second fraction of affixed particles behind in the second location B. This process was continued to acquire fractions at 625 and 650 psi at positions C and D respectively. A final precipitation at 700 psi can induce the precipitation of the remaining particles from the hexane dispersion at location E in the spiral tube.

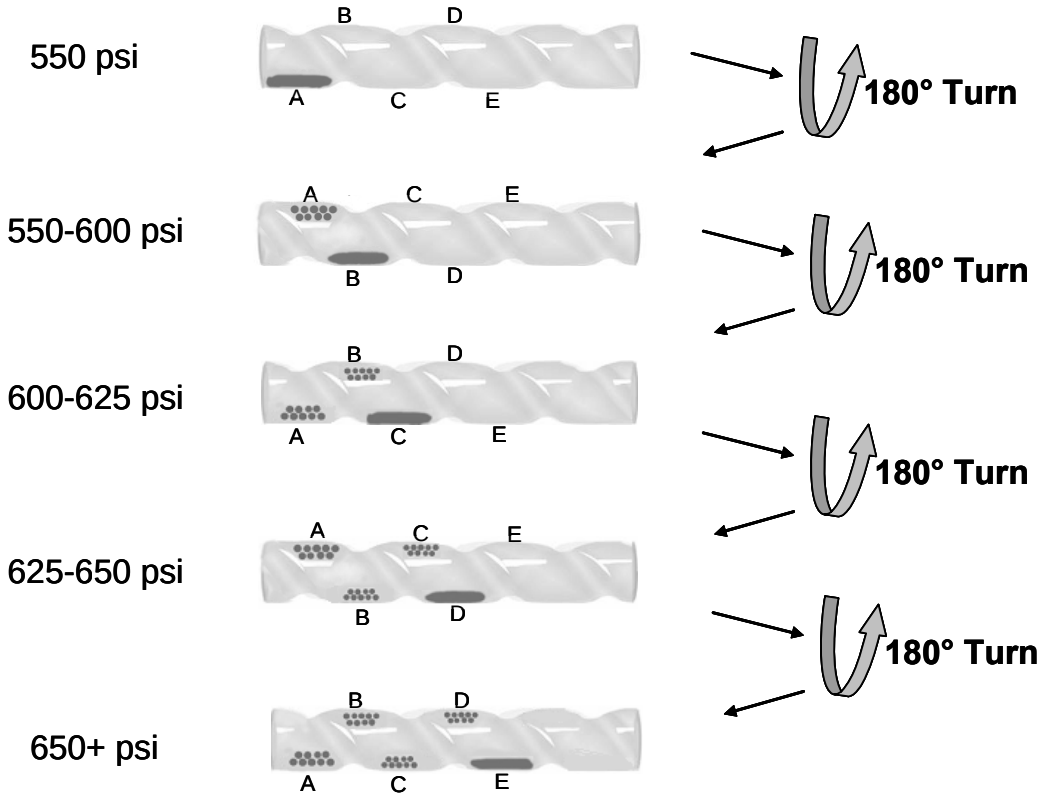

Figure 2. Nanoparticle size selection spiral tube apparatus depicting recursive pressurization of organic liquid with CO_2, followed by 180° tube rotations to achieve multiple size selected populations.

Sample Collection. After completing the final precipitation, the vessel was depressurized. There were 5 particle populations in the spiral tube at locations A, B, C, D and E. These 5 particle samples were recovered through redispersion in hexane, giving 5 size fractions. Sample grids were made by evaporative deposition and tested for particle size distribution on a Zeiss EM 10 Transmission Electron Microscopy (TEM).

Volume Expansion of the Solution. When a given organic dispersion of nanoparticles was pressurized with CO_2, the volume of the organic phase was increased by dissolution of CO_2 until equilibrium was reached. This increase in volume of the organic dispersion/CO_2 mixture can be characterized by the volume expansion coefficient, defined as $\frac{(V - V_0)}{V_0}$, where V is the volume of the solution saturated with CO_2 at a given pressure and V_0 is the volume of the CO_2 free solution (unpressurized). This volume expansion coefficient was estimated using the Peng-Robinson equation of state[5] and compared well to measurements made by visual observation of volume expansion in a high pressure Jerguson site gage (less than 5% error between the experimental data and the equation of state in the pressure range of 500 to 700 psi).

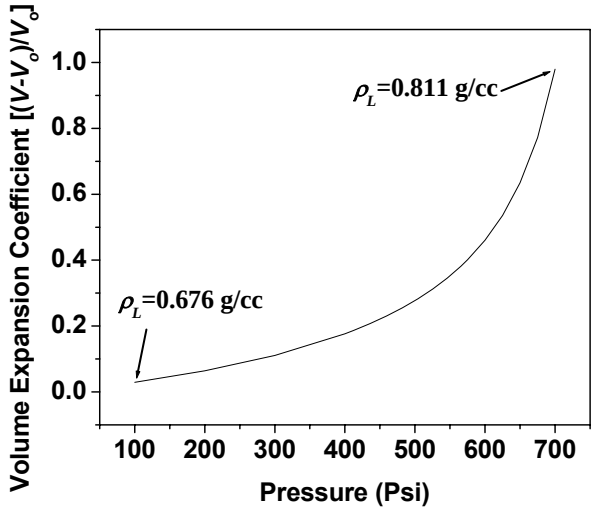

Figure 3. Volume expansion coefficient vs. system pressure for liquid hexane/CO_2 mixtures pressurized with gaseous CO_2 and modeled using the Peng-Robinson equation of state at 25°C.

This volume expansion coefficient is necessary when interpreting UV-Visible spectra to compensate for the decrease in particle concentration that accompanies an increase in solution volume with CO_2 pressure. The volume expansion coefficient of hexane for a range of CO_2 pressures as determined by the Peng-Robinson equation of state, is shown in Figure 3 where increases in CO_2 pressure significantly increase the volume expansion coefficient as a result of CO_2 gas partitioning into the liquid phase. Interestingly, this dissolution of CO_2 in the organic solvent also increases the density of the solvent mixture as obtained from the Peng-Robinson equation of state, indicating that while these mixtures are referred to as gas expanded liquids, the resulting solution is a dense mixture of liquid CO_2 and organic solvent. However, CO_2 is a very poor solvent for the solvation of the ligand coated particles in the organic solvent mixture. Therefore, as the percentage of CO_2 increases in the expanded organic solvent, solvent-ligand interactions decrease and the dispersed particles will precipitate once a threshold solvent strength is passed.

UV-Visible Absorbance Spectroscopy. An increase in CO_2 pressure decreases the concentration of dispersed nanoparticles. This is due to a decrease in the solvent strength of the GEL. Here, a decrease in solvent strength means that CO_2 has a very poor interaction with the ligand tails attached to the nanoparticles as compared to the organic solvent. So, as the concentration of CO_2 in the GEL is increased, interactions between the ligand tails and the solvent is diminished such that particles are no longer stabilized and start precipitating from the solvent. The precipitation of the nanoparticles from the organic solvent depends on many factors, such as ligand type, solvent type, temperature, and metal type. The effect of each of these variables on the nanoparticle precipitation process is being examined.

Figure 4 presents the UV-vis spectra of gold particles synthesized by arrested precipitation and dispersed in hexane (top line).

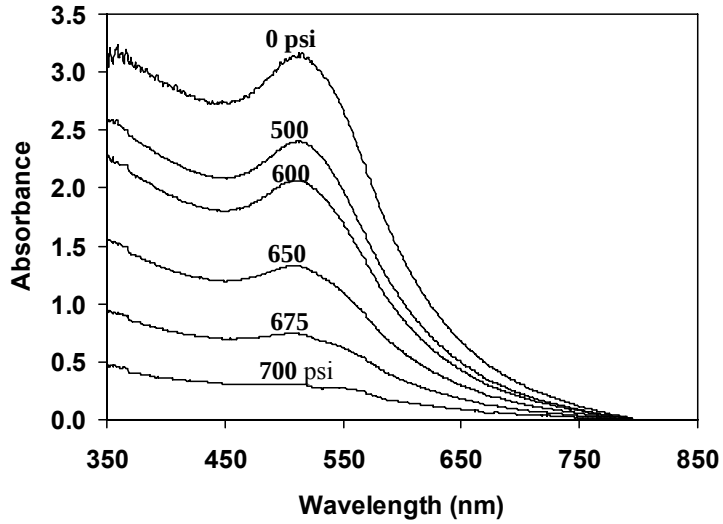

Figure 4. UV-visible absorbance spectra of gold particles dispersed in hexane/CO_2 liquid mixtures at increasing CO_2 pressures. The spectra were normalized to give zero absorbance at 800 nm wavelength. Decreased absorbance of gold particles after correcting for the volume expansion of hexane shows that particles are precipitating from hexane by increasing the CO_2 pressure.

This absorption band is attributed to the absorption of Au nanoparticles dispersed in hexane and is due to the excitation of plasma resonances or interband transitions[6]. The gold nanoparticles do not precipitate in the absence of CO_2 even after extended periods of time. However, the intensity of the UV absorbance band decreases when the nanoparticle dispersion was pressurized with CO_2. This decrease in intensity indicates that particles begin precipitating from solution and the absorbance maximum decreases with the increase in pressure. Correspondingly, the absorbance maxima of the UV-Visible spectra, after correcting for the volume expansion of the organic solvent with the addition of CO_2, was plotted against the CO_2 pressure as a measure of particle concentration that remains dispersed at a given CO_2 pressure.

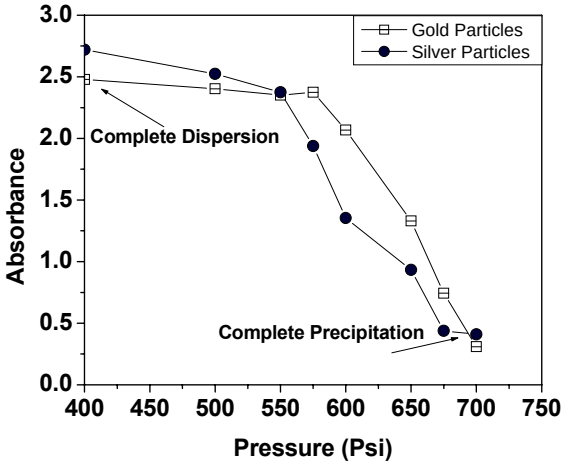

Figure 5. Maximum UV-visible absorbance of dodecanethiol coated silver[3] and gold particles dispersed in liquid hexane/CO_2 mixtures vs. system pressure. Absorbance values obtained were corrected for the volume expansion of the liquid mixture.

Figure 5 shows a decrease of the absorbance with an increase in the pressure of CO_2 and indicates that the gold nanoparticles primarily precipitate from the solution in the range of 500 to 700 psi of CO_2 pressure. At pressures higher than 700 psi, complete precipitation occurs. The gold particles used in this experiment had a mean particle size of 5.0 nm and a standard deviation of 26% as shown in Table 1. McLeod et al.[3] also demonstrated a dramatic decrease in the UV absorbance band for dodecanethiol stabilized silver particles dispersed in hexane with similar increases in CO_2 pressure (also shown in Figure 5). The mean particle size and standard deviation for these silver particles[3] was 5.5nm and 31.9%, respectively. Interestingly, the pressure range for the precipitation and the slope of this curve was very similar for both the gold and silver nanoparticles. This is consistent with the fact that both dodecanethiol stablizied gold[7] and dodecanethiol stabilized silver[8] nanoparticles have Hamaker constants of 1.95eV resulting similar inherent van der Waals forces of attraction.

TEM Characterization. The particle size precipitated at each pressure range was determined by analysis of TEM images using ImageJ software where each particle was bounded by a rectangle and the diameter was estimated by the average of length and width of the rectangle. Figure 6 (A) shows an example of the TEM micrographs of unprocessed dodecanethiol-coated gold particles prepared by the two phase arrested precipitation method as explained earlier. These images were analyzed to determine the size distribution of this original sample as shown in Figure 6(B). This original sample of polydisperse dodecanethiol-coated gold particles was fractionated in a spiral tube into 5 fractions corresponding to different pressure ranges at different locations in a spiral tube as shown by arrows in Figure 7. TEM images of these fractions given in Figure 7 illustrate that the particle size collected within each ΔP decreases with increased CO_2 pressure.

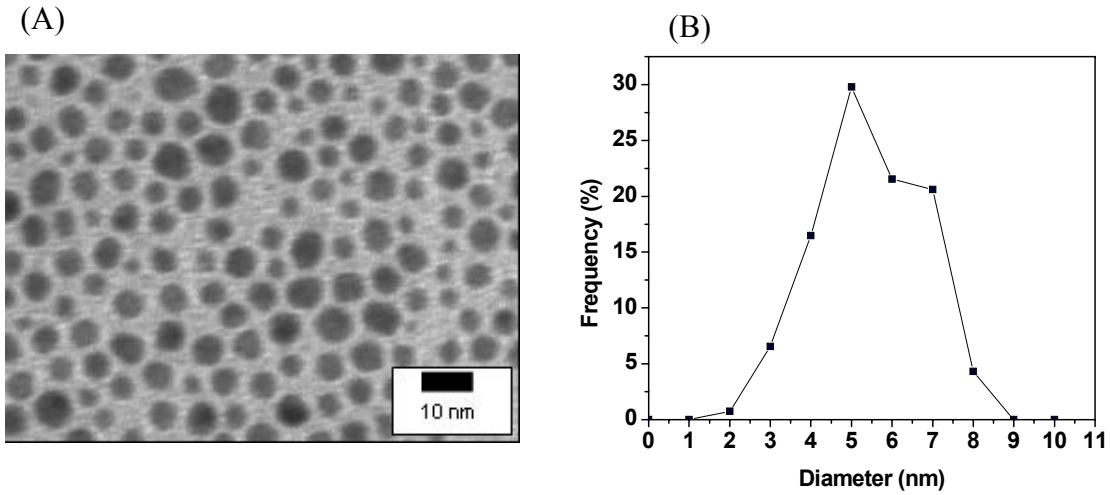

Figure 6. (A) TEM micrograph of unprocessed dodecanethiol-coated gold particles prepared by two phase arrested precipitation method. (B) Size distribution of unprocessed particles.

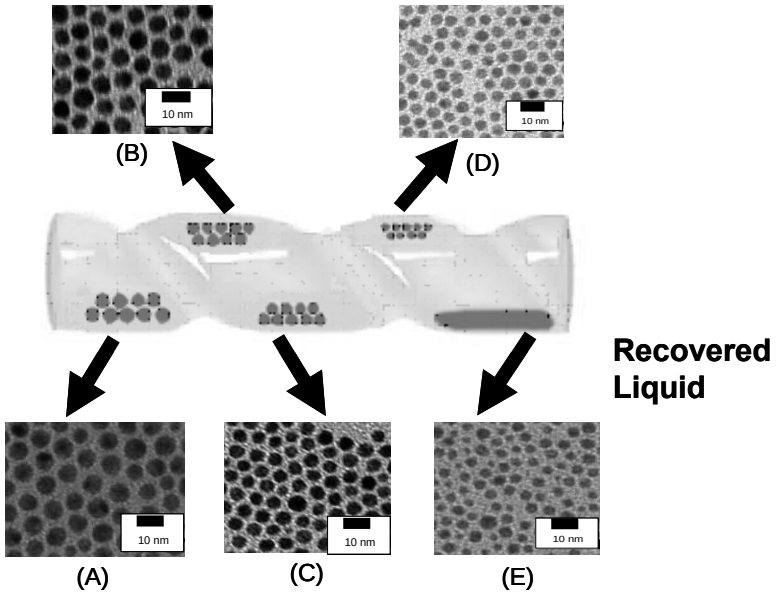

Figure 7. TEM micrographs of particles precipitated from hexane by CO_2 pressurization from (A) 0 to 550 psi, (B) 550 to 600 psi, (C) 600 to 625 psi, (D) 625 to 650 psi and (E) 700 psi CO_2 pressurization.

Moreover, particles in these images are very monodisperse and significantly more ordered into arrays as a result of the size separation process. After analyzing these particles with ImageJ software, histograms were prepared for all 5 pressure ranges simultaneously as shown in Figure 8 to quantitatively compare the various fractions. Compared to the wide size distribution (Figure 6(B)) of the original sample ranging from (2-9 nm), the histograms of the distinct fractions obtained after the size separation process are sharp (±2 nm). The size separation process improves the quality of the particles by increasing the percentage of particles at the median particle size in a single experiment. For example, 30% of the original group of nanoparticles was 5 nm in diameter but after the size separation process, 70% of the

particles in the 650 psi fraction were 5 nm. Table 1 shows a statistical analysis of the fractions obtained at different pressure ranges from the size selection process. The standard deviation of the original sample is 26%. At 550 psi, the standard deviation is 22.4% because the pressure range, ΔP for collection, is large (0 to 550 psi). The standard deviation was reduced to 15.9% for the particles precipitated from 550 to 600 psi with a ΔP of 50 psi. The standard deviation was further reduced to 12.5% at 625 psi and 11.0% at 650 psi with ΔP's of 25 psi in each of these fractionation steps. This illustrates that a smaller ΔP from the same starting P gives a more precise particle separation due to a more subtle change in solvent strength and the process can be manipulated to obtain a desired particle size. McLeod et. al.[3] showed that pressure can be used as a parameter to obtain a desired particle size. McLeod et. al. also showed that smaller pressure changes (ΔP) from the same starting P for precipitation can be used to further narrow the size distribution where a ΔP of 50 psi resulted in a standard deviation of 16.1% and a ΔP of 6 psi resulted in a standard deviation of 14.7% for silver particles.

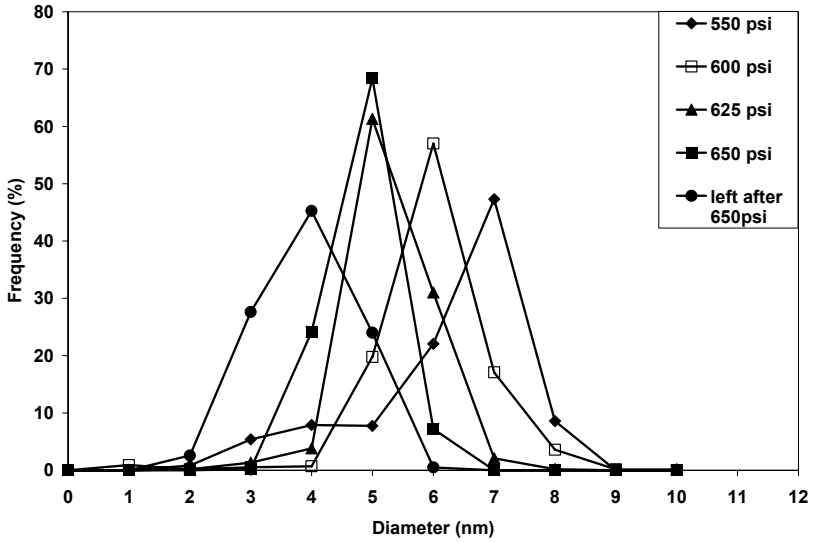

Figure 8. Size distributions of dodecanethiol-coated gold particles fractionated within the CO_2 pressure ranges of 0-550 psi (diamond), 550-600 psi (open square), 600-625 psi (triangle), 625-650 psi (closed square), 700 psi (circle). Data points represent the percentage of particles of the total population found between the associated diameter and <1nm less than that diameter.

Fraction (Psi)	ΔP of Fraction (Psi)	Mean Diameter (nm)	Std Dev (nm)	Relative Std Dev (%)	95% Confidence (nm)	Particle Count
Original	0	5.0	1.3	26.0	0.1	534
0 to 550	550.0	5.7	1.3	22.4	0.1	594
550 to 600	50	5.5	0.9	15.9	0.07	556
600 to 625	25	4.8	0.6	12.5	0.05	522
625 to 650	25	4.3	0.5	11.0	0.04	459
650 +	<50	3.4	0.7	20.6	0.06	579

Table 1. Statistical analysis of particle populations where the five fractions were separated in a single experiment from the original population. All gold particles are completely precipitated from the hexane at 700 psi.

Effect of Solvent Hydrocarbon Length on the Size Selective Precipitation Process. Kitchens et al[9]. explained that variations in bulk solvent strength can have a significant effect on the size of nanoparticles that can be sterically stabilized in a given solvent. For example, cyclohexane solvent was shown to disperse larger AOT (sodium bis(2-ethylhexyl)sulfosuccinate) stabilized copper nanoparticles than was hexane solvent at identical operating conditions as a result of stronger AOT-solvent interactions. Shah and coworkers also demonstrated that the dispersability of dodecanethiol stabilized gold and silver particles could be varied in liquid and supercritical ethane by altering the pressure and thereby tuning the solvent density[10]. Moreover, variations in solvent strength can play an important role in the precipitation and deposition[11,12] processes of particles. For example, Sigman and coworkers examined the morphology of dodecanethiol stabilized gold and silver nanocrystal thin films that were deposited from various solvents and they attributed the morphology changes to the different interparticle attractions in the organic solvents[12]. Rough superlattice films were obtained from hexane, while smooth films were deposited from chloroform. Each of these works demonstrate that the interactions between the solvent and the particle stabilizing ligands play an important role in the dispersion and precipitation of nanoparticles. In general, a decrease in the solvent strength weakens the solvation of the ligand tails and results in stronger tail-tail interactions[13] thereby decreasing the particle dispersability. Sufficient solvation of the thiol stabilizing ligand tails is necessary to provide enough repulsive force (osmotic and elastic repulsion) to overcome the van der Waals forces of attraction between the nanoparticles.

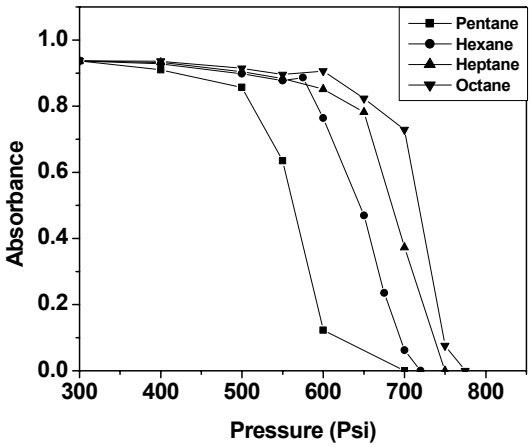

Figure 9. Maximum UV-visible absorbance values for dodecanethiol coated gold nanoparticles dispersed in different hydrocarbon length solvents pressurized with CO_2.

The effect of different solvents on the size selective precipitation and fractionation process was examined. Figure 9 presents maximum UV-visible absorbance values for dodecanethiol coated gold nanoparticles dispersed in different hydrocarbon length solvents pressurized with CO_2. These absorbance maxima were normalized to a common initial value for ease of comparison and zero absorbance simply denotes that all the particles were precipitated from solution at that pressure. In hexane, a large percentage of the particles remained dispersed up to 550 psi after which point more appreciable precipitation occurred (precipitation of successively smaller particles) with further increases in CO_2 pressure until all the particles had precipitated at 725 psi and beyond. In contrast to hexane, pentane is a slightly weaker solvent, and as such, appreciable precipitation was initiated at only 400 psi with complete precipitation as low as

700 psi. Given that pentane provides weaker solvation of the ligand tails than hexane, smaller amounts of CO_2 are necessary to bring the solvent/CO_2 mixture solvent strength below the threshold for dispersability of a given particle size. As a result, the pressure range required for precipitation is less in pentane than hexane. Interestingly, heptane and octane both exhibit stronger interactions with the ligand tails as compared to hexane resulting in more stable dispersions in the longer chain length solvents. Correspondingly, greater CO_2 pressure is required to reach the same weakened solvent strength of the solvent/CO_2 mixture to induce precipitation of nanoparticles of a given size. Figure 9 shows that the length of the organic solvent influences the gold nanoparticle precipitation process where the longer length solvent molecules have stronger interactions with the nanoparticle ligand tails compared to the shorter length solvent molecules. Additional results of similar experiments performed with cyclohexane, decane, isooctane, and toluene are not shown here in Figure 9. In these solvent systems, particle dispersability remained quite high even at CO_2 pressures approaching the vapor pressure of CO_2 where the dodecanethiol coated gold particles remained dispersed in the solvent/CO_2 mixtures for several hours.

Effect of Thiol Length on the Size Selective Precipitation Process. Martin et al.[14] states that among all the alkyl thiols, dodecanethiol is more strongly bound to gold particles than hexanethiol or hexadecanethiol. Prasad et al.[7] studied the effect of the alkyl chain lengths of thiol molecules on the formation of gold nanoparticle superlattices. These authors describe that there is a decrease in particle-particle attraction energy with an increase in the thiol hydrocarbon chain length. For example, particles aggregated into 3D superlattices with short chain lengths, i.e octanethiol and decanethiol (C_8 and C_{10}), due to particle-particle attraction. Longer chain length in hexadecanethiol resulted in weakly bound multilayers and hinders the development of 3D superlattices. These works have demonstrated the impact of thiol chain length on particle-particle attraction. It is important to note that in the current study, dispersion of particles in solution requires that these attractive interactions be finely balanced by the osmotic repulsion and an elastic contribution generated by interactions between the solvent and the thiol stabilizing ligands. As shown in the previous section of this paper, modification of the solvent strength of the solution (i.e. CO_2 pressurization) can result in changes in these attractive and repulsive interactions thereby inducing precipitation. Changes in this fine balance can also be accomplished by altering the thiol chain length such that there is a modification to the interaction between the solvent and the thiol ligand tails. Here we present the influence of various thiol chain lengths on the CO_2 pressurization range required to induce precipitation. As shown in Figure 10 precipitation of the particles stabilized with octanethiol ligands occurs between 400 and 600 psi as compared to 400 to 700 psi for particle stabilized by dodecanethiol ligands. The precipitation of particles with hexanethiol ligands was similar to those with octanethiol ligands, and the curve was shifted to a lower pressure range (300-575 psi). Particles stabilized with tetradecanethiol ligands require a smaller CO_2 pressure for the precipitation of particles compared to dodecanethiol ligands, even though they have a longer tail length. The shorter tail length for octanethiol and hexanethiol ligands decreases the CO_2 pressure required for precipitation in a GEL compared to dodecanethiol ligand stabilized particles. This effect is because the shorter length ligands have smaller interactions with the solvent compared to the longer length ligands. Tetradecanethiol ligand stabilized particles also require less CO_2 pressure for the nanoparticle precipitation than dodecanethiol ligand stabilized particles because of larger tail - tail interactions. Our results here suggest that dodecanethiol

ligands have the optimum length for strong ligand – solvent interactions similar to observations made by Prasad et al.[7]

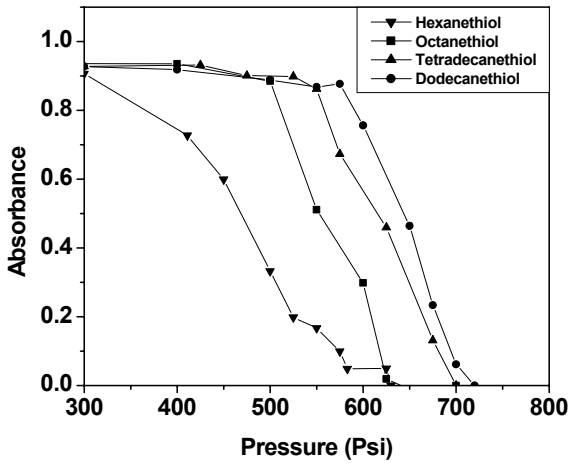

Figure 10. Maximum UV-Visible absorbance values for gold nanoparticles coated with different thiol length molecules dispersed in liquid hexane/CO_2 mixtures at increasing CO_2 pressure.

Effect of Temperature on the Size Selective Precipitation Process. Temperature also has a pronounced effect on nanoparticle stabilization and dispersibility. Temperature affects solvent density, and as such, also affects the nanoparticle dispersability in an organic solvent. The effect of temperature on the precipitation of gold particles stabilized with dodecanethiol ligands in hexane are shown in Figure 11. At the lowest temperature of 22 ^{o}C, the nanoparticle precipitation occurs between 500 and 700 psi CO_2 pressure. At the highest temperature of 35 ^{o}C, this pressure range for precipitation was shifted up to 650 to 800 psi, illustrating that an increase in pressure is required for precipitation with an increase in temperature. This variation is due in part to the CO_2 density change with temperature. As temperature is increased, the mole fraction of CO_2 in the organic liquid/CO_2 mixture is reduced resulting in a smaller volume expansion of the liquid dispersion at a given pressure. This, therefore, reduces the antisolvent effect in the nanoparticle precipitation process.

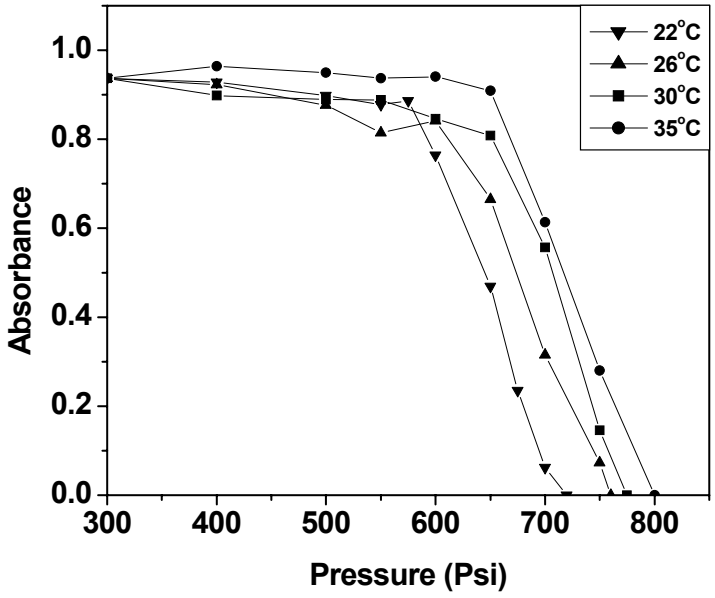

Figure 11. Maximum UV-Visible absorbance values for dodecanethiol coated gold nanoparticles dispersed in liquid hexane/CO_2 mixtures at various CO_2 pressures and system temperatures.

Recursive Fractionations. Recursive fractionation of a given system within a particular pressure range (solvent strength) further reduces the polydispersity of the fraction obtained within that pressure range. Korgel and coworkers used ethanol recursively as an antisolvent to improve the size separation process. In the current study, a set of size separation experiments were repeated on one of the recovered fractions (particles collected within a given pressure range at one location in the spiral tube) to further improve the size separation process using CO_2 as an antisolvent. The results of the recursive fractionation are summarized in Figure 12. The size separation process, shown above, was done by placing the original polydisperse sample at location A in the spiral tube. The 1st fractionation sample, at location D, was the sample of particles precipitated within the pressure range of 625-650 psi. In this recursive process, this 1st fractionation sample was collected at the end of the experiment and was returned to location A and the size separation process was repeated. The 2nd fractionation sample was again obtained from position D within the same pressure range of 625-650 psi. In the same way, the 3rd fractionation was obtained by placing the 2nd fractionation sample at location A and collecting the particles precipitated at location D within the same pressure range. The separation was improved during each successive processing step with a decrease in the standard deviation from 13% to 8% as shown in Table 2. This process is an improvement over the liquid antisolvent process where the desired size is controllably obtained as a function of pressure. For instance, keeping the solvent, thiol length and temperature the same, this process will always result in a ~5.0 nm sized fraction of gold particles collected at 650 psi since the precipitation is governed simply by the solvent strength. Therefore, this CO_2 antisolvent size separation process gives a predictable particle size at a given CO_2 pressure. On the other hand, the number of variables involved in the liquid antisolvent process including the

specific amount of ethanol addition and the centrifugation time makes predictable size selection challenging.

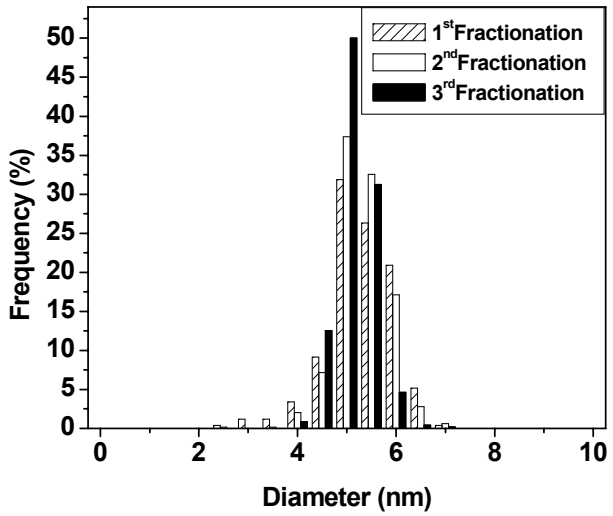

Figure 12. Comparison between the size distributions of gold particles collected in the pressure range of 625 to 650psi after fractionation one, two or three times. Particles from the 1st fractionation were obtained from the location D in the spiral tube apparatus corresponding to pressure range of 625-650 psi. This 1st fractionation sample was returned to location A and the size separation process was repeated. The 2nd fractionation sample was again obtained from position D. In the same way, the 3rd fractionation was obtained by placing the 2nd fractionation sample at location A and collecting the particles precipitated at location D. Data points represent the percentage of particles of the total population found between the associated diameter and <0.5 nm less that diameter.

Fractionation (Number)	Mean Diameter (nm)	Std Dev (nm)	Relative Std Dev (%)	Fraction (Psi)	95% Confidence (nm)	Particle Count (nm)
1	5.0	0.7	13.1	625-650	0.06	502
2	5.0	0.5	10.0	625-650	0.04	642
3	4.9	0.4	8.1	625-650	0.04	454

Table 2. Statistical analysis of particle populations for different numbers of fractionation steps.

Effect of Time on the Size Selective Precipitation Process. During this size selection process, the liquid droplet with dispersed nanoparticles is moved to a specific location on the surface of the spiral tube followed by an increase in pressure that initiates precipitation of particles within that pressure range. Once the desired pressure is reached, the system is allowed to sit for a specified period of time allowing precipitation of the particles, and this period of time is referred to as the holding time. Table 3 presents standard deviations for

particles precipitated during three different holding times in the pressure range of 600-625 psi. The results shown earlier in this paper were collected during a holding time of 20 min where a mean size of 4.7nm and the standard deviation of 14.9% were obtained as given in Table 3. For holding time of 1 hr, the mean size and standard deviation were 4.7nm and 16.9% respectively. It was found that a 5 min holding time resulted in a standard deviation of 14.6% with a mean nanoparticle size of 5.1 nm. The experiments performed at different holding times suggest that there is little difference in the size distribution of the nanoparticles collected indicating that the system quickly reaches an equilibrium. This demonstrates that the size separation process using CO_2 as the antisolvent is a very rapid process compared to the liquid antisolvent process which requires several hours for the separation of the same quantity of particles.

Holding Time (min)	Mean Diameter (nm)	Std Dev (nm)	Relative Std Dev (%)	95% Confidence (nm)	Particle Count (nm)	Fraction (Psi)
5	5.1	0.75	14.6	0.06	464	600 to 625
20	4.7	0.70	14.9	0.07	309	600 to 625
60	4.7	0.79	16.9	0.06	591	600 to 625

Table 3. Statistical analysis of particle populations for different holding times at each step of fractionation.

Process Development for Size Selective Precipitation of Semiconductor Nanoparticles

Semiconductor nanoparticles (also known as quantum dots) have unique electronic and optical properties due to the three dimensional confinement of charge carriers. The change in properties for quantum dots, 10 nm or less in size, results from confinement of holes and electrons into a dimension which is close to a critical quantum measurement called exciton Bohr radius. Extensive research has been performed to study the size dependent quantum confinement of semiconductor quantum dots. The valence–conduction band-gap increases in semiconductor nanoparticles with a decrease in the particle diameter and therefore provides an avenue for size-tunable nanodevices. The properties of semi conductor nanoparticles, such as the electronic states, light absorption, and emission, can be tuned with particle size and shape. As such, monodisperse semiconductor nanoparticles are employed in number of applications such as optoelectronic devices, sensors, telecommunications, catalysis and as fluorescent chemical labels in biomedicine. CdSe is one the most widely used semiconductor nanocrystal materials due in part to the availability of highly efficient and high quality CdSe nanoparticle synthesis techniques and the fact that their optical gap is in the visible region.

Much research has been done to develop efficient synthesis as well as post-synthesis processing techniques to produce semi-conductor nanocrystals with narrow size distributions. A number of synthesis techniques for semi-conductor nanocrystals have been reported including arrested precipitations, microemulsion methods, reverse micelle based synthesis technologies, high-temperature pyrolysis, sonochemical, and radiolytic methods. One of the most efficient techniques to synthesize CdSe nanocrystals is through kinetically controlled

precipitations where CdSe nanocrystals are stabilized with capping ligands like trioctyl phosphine oxide (TOPO).

While several synthesis alternatives have been developed for semiconductor nanoparticles, post-synthesis purification and size-separation processing steps are commonly required to obtain nanoparticle fractions with desired size and narrow size distributions. Various post-synthesis processing steps such as liquid antisolvent precipitation and exclusion chromatography have been developed that allow tight control over particle size and polydispersity to finely tune the properties of the semiconductor nanoparticles. Perhaps the most widely applied technique involves liquid antisolvent induced size-selective precipitations coupled with centrifugation. In this liquid antisolvent precipitation technique, ligand capped nanocrystals are first dispersed in a solvent. An antisolvent is introduced dropwise to this stable nanoparticle dispersion until opalescence occurs upon stirring. This addition of antisolvent weakens the ligand-solvent interaction and thus results in precipitation of nanoparticles where particles of decreasing size precipitate with the gradual addition of the antisolvent. The solution is normally centrifuged after each addition of antisolvent to speed up the precipitation process for the unstabilized fraction of the particles in solution. This process of gradual antisolvent addition and centrifugation is repeated a number of times on the precipitate or supernatant depending on how narrow a size distribution is required. Although this liquid antisolvent process is commonly employed, it is time consuming, solvent intensive, and requires multiple processing steps. This technique is also somewhat subjective in that the separation depends on the observation of opalescence during antisolvent addition. Improved size-selective precipitation techniques are required to address these limitations and during this quarter we have applied our unique size separation technique to semiconductor particles while also working on scaling up the process.

Materials for Semiconductor Nanoparticles. The four different sized CdSe/ZnS core shell nanoparticles capped with TOPO and dispersed in toluene were purchased from Evident Technologies. Hexane (99%) was obtained from Aldrich chemical Co. and Carbon dioxide (SFC/SFE grade) was obtained from Airgas. All chemicals were used as received. CdSe/ZnS core shell quantum dots were chosen for investigation because the ZnS core shell improves stability, strength and fluorescent brightness of the CdSe quantum dots. The TOPO capped CdSe/ZnS core shell quantum dots which were dispersed in toluene were of four different colors; red, orange, yellow and green corresponding to average crystal diameters 5.2 nm, 3.2 nm, 2.4 nm, 1.9 nm respectively. The mixture of these 4 different sized semi-conductor nanoparticle dispersions in toluene were prepared from equimolar quantities as shown in vial named original of Figure 13.

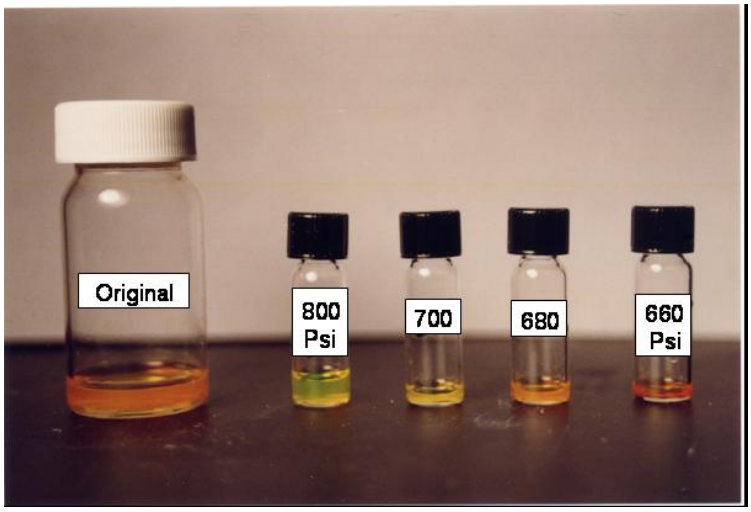

Figure 13. A mixture of four different sizes of CdSe/ZnS core shell nanoparticles capped with TOPO and dispersed in hexane in equimolar quantities as shown in vial named original was size separated using CO_2 gas expanded liquids into their real four different sizes/colors.

Solvent Exchange. An earlier study on the CO_2 gas expanded liquid size precipitation process has demonstrated that the solvent used for the bulk medium has a significant impact on the pressure range required for precipitation of metal nanoparticles capped with alkane thiol ligand tails. Stronger interactions between the solvent and the hydrocarbon ligand tails required greater CO_2 pressure to precipitate the particles. Previous studies indicate that toluene is a very good solvent for hydrocarbon ligand tails and particle dispersability in this solvent medium remains quite high even at CO_2 pressures approaching the vapor pressure of CO_2. For instance, dodecanethiol coated gold nanoparticles remain dispersed in toluen/CO_2 mixtures for several hours. Similarly, in the current study TOPO capped CdSe/ZnS core shell quantum dots remained dispersed in toluene even at the vapor pressure of CO_2 for several hours rendering the toluene medium inappropriate for the CO_2 gas expanded liquid precipitation process. The solvent medium for the mixed CdSe/ZnS core shell quantum dot dispersions was changed from toluene to hexane by completely evaporating toluene and subsequently dispersing the particles in hexane. Hexane has a lower solvent strength than toluene and resulted in significant CdSe/ZnS particle precipitation when the hexane medium was pressured with CO_2 up to its vapor pressure.

Size Selective Precipitation Process for Semiconductor Nanoparticles. The mixed CdSe/ZnS core shell quantum dots were separated into distinct size fractions (different colors) via CO_2 pressure induced size selective precipitation at specific locations on the surface of a spiral tube apparatus as shown in Figure 1 This spiral tube precipitation apparatus consists of an open ended glass tube (2cm diameter, 12 cm long) modified to include a concentric, spiral indentation on the surface of the tube from one end to the other. These spiral indentations provide a spiral channel (6mm deep, 2.5 cm wide each) or groove inside of the tube that allows a liquid droplet of the nanoparticle dispersion resting within the channel to be translated from one location to another by a simple rotation of the tube while keeping the length of the tube horizontal. In short, the function of the spiral tube is like that of an Archimedes screw, where the liquid nanoparticle dispersion can be controllably moved from one location within the

groove to the next by simple rotation of the tube. This spiral tube is located within a cylindrical stainless steel high pressure view cell equipped on one end with an O-ring sealed quartz window that allows observation of the liquid expansion and particle precipitation process. The other end of the high pressure cell is fitted with a Teflon high pressure fitting that allows the entry of a 1/8 in. stainless rod connected to the spiral tube with a Teflon interconnect. This interconnect assembly allows radial rotation of the spiral tube within the high pressure vessel by simply turning the metal rod outside the vessel while maintaining the dynamic high pressure seal with the Teflon fitting. Thus, the location of liquid droplet of nanoparticle dispersion in a spiral tube can easily be controlled by simply turning the steel rod from outside the vessel while maintaining the high pressure conditions within the vessel. The spiral groove within the tube also helps in separating the liquid nanoparticle dispersion from an already precipitated nanoparticle particle fraction by moving the remaining liquid dispersion to the next desired location along the length of the tube. Therefore, by placing a sample of the mixed nanoparticle dispersion at one end of the spiral tube, and by coordinating sequential increases in the CO_2 pressure along with movement of the liquid to the next location within the tube prior to each pressurization step, successively smaller sized nanoparticles can be precipitated at each subsequent location on the tube surface.

An experiment was started by placing 700μL of pure hexane in the annular space outside the spiral tube in the high pressure vessel and allowing it to sit for 10 minutes to saturate the vessel with hexane vapor. This prevents the excessive evaporative loss of hexane from the original hexane nanoparticle dispersion which was introduced later in the spiral tube within the high pressure vessel. Next, 250μL of the original mixed nanoparticle dispersion in hexane was placed in the spiral grove at location A closest to the quartz window, as shown in the top image of Figure 3. The vessel was then slowly pressurized to an initial pressure of 660 psi with CO_2 gas using an ISCO 260D syringe pump. Once the desired pressure was reached, the system was allowed to sit for 20 minutes to allow the largest size fraction of the CdSe/ZnS core shell nanoparticles to precipitate. The increase in CO_2 pressure at 660 psi results in an increase in the concentration of CO_2 within the hexane nanoparticle dispersion (CO_2 expanded hexane solution) where the condensed CO_2 acts as an antisolvent thereby causing the largest fraction of the CdSe/ZnS core shell nanoparticles that are no longer stabilized in the weakened CO_2/hexane mixture to precipitate at location A as shown in Figure 14. This preciptated fraction of the CdSe/ZnS nanoparticles adhered to the surface of the spiral tube at location A through van der Waals forces of attraction with the surface. To move the remaining dispersion away from affixed particles, the spiral tube was rotated by turning the metal rod 180^o. This rotation of the spiral tube moved the liquid dispersion to the next location, B, leaving the largest size fraction of the particles, those that were precipitated at 660psi, affixed to the spiral tube at location A. The residual liquid nanoparticle dispersion, now located at location B within the spiral tube, was further subjected to the next higher CO_2 pressure, 680psi, and allowed to sit for 20 minutes to allow additional condensed CO_2 to mix with the nanoparticle dispersion and, hence, induce the second largest size fraction to precipitate. This sequence of pressurization, precipitation and movement of the remaining liquid nanoparticle dispersion to the next location in the spiral tube, was repeated with CO_2 pressures of 700 and 800 psi resulting in nanoparticle precipitation of subsequently smaller size fractions at locations C & D in the spiral tube, respectively. In the end, four different colored fractions of the original CdSe/ZnS core shell quantum dot dispersion in hexane with TOPO as capping ligand were recovered from this CO_2 expanded liquid separation process.

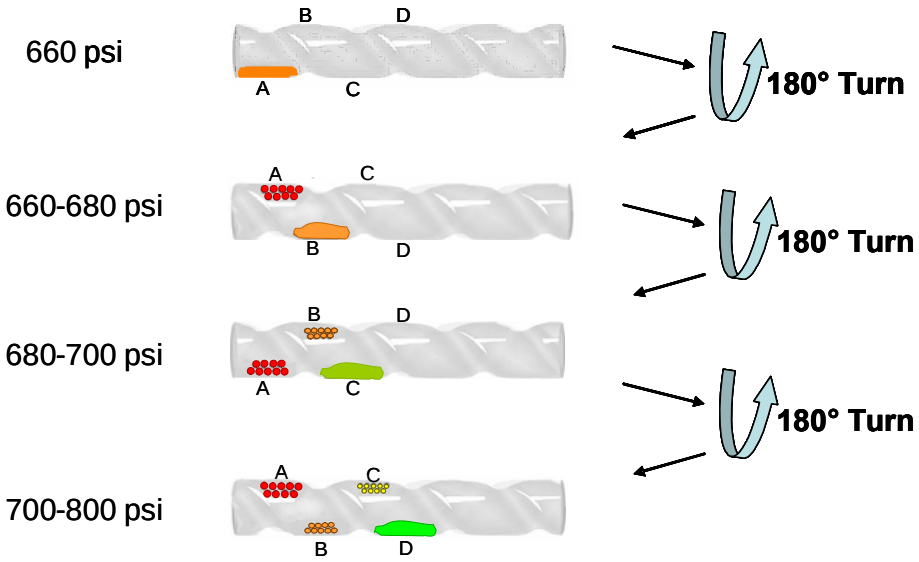

Figure 14. Nanoparticle size selection spiral tube apparatus depicting recursive pressurization of organic liquid with CO_2, followed by 180° tube rotations to achieve multiple size selected populations.

Semiconductor Particle Sample Collection. After completing the final precipitation, the vessel was depressurized. The four recovered fractions of the CdSe/ZnS core shell nanoparticles were redispersed in hexane and displayed four distinct colors (red, orange, yellow and green), as shown in Figure 13, corresponding to the four samples used in making the original mixed nanoparticle dispersion. In the end, four different colored fractions of the original CdSe/ZnS core shell quantum dot dispersion in hexane with TOPO as capping ligand were recovered from this CO_2 expanded liquid separation process. This result demonstrates that monodisperse fractions of CdSe/ZnS core shell quantum dots can be separated and recovered from a mixture of multiple sized CdSe/ZnS nanoparticles in a single process by using an efficient size separation technique based on the pressure tunable physicochemical properties of CO_2 gas expanded liquids.

Semiconductor Particle UV-Visible Absorbance Spectroscopy. These redispersed CdSe/ZnS nanoparticles after the size separation process were further analyzed using UV-vis spectroscopy and TEM. Figure 15 shows the UV–visible absorbance spectra of the four samples of TOPO capped CdSe/ZnS core shell quantum dots dispersed in hexane before they were mixed and subsequently size-separated. A quartz cuvette of 10 mm path length was filled with 160μL of the dispersed nanoparticles in hexane and the UV-vis absorbance spectrum of each sample was collected using a Varian 300E spectrophotometer with absorbance measurements acquired at wavelength intervals of 1nm over the range of 200 to 800 nm. It is clear from Figure 15 that the absorbance spectra of the CdSe/ZnS nanoparticles is a strong function of particle size. For example, the red colored line in Figure 15 corresponds to the sample with an average crystal diameter of 5.2 nm having a wavelength of maximum absorption of 594 nm (which also corresponds to a red colored dispersion). Similarly for the orange, yellow and green colored dispersions, corresponding to average crystal diameters of 3.2 nm, 2.4 nm, 1.9 nm, the wavelengths of maximum absorption were observed at 563, 522 and 475, respectively. Four dotted lines were added to Figure 15 corresponding to these wavelengths of maximum absorption for the four different sized CdSe/ZnS nanoparticles.

Equal amounts of these four nanoparticle dispersions in hexane were then mixed to produce a CdSe/ZnS nanoparticle dispersion consisting of four distinct nanoparticle size populations (average diameters ca. 5.2 nm, 3.2nm, 2.4nm, and 1.9nm) in hexane. This mixture of the original samples (now referred to as 'original sample') was then subjected to particle separation (nanoparticle size fractionation) using the CO_2 gas expanded size separation technique. The UV-vis absorbance spectrum of this original sample is presented as a solid line in Figure 16. On the other hand, the dashed line in Figure 16 corresponds to the cumulative spectrum obtained by adding of the absorbances at each wavelength from the four different spectra in Figure 15 corresponding to the four different colored dispersions (adjusted to zero absorbance at 800nm).

The primary absorbance bands in both the spectrum of the original sample mixture and cumulative spectrum correspond to the wavelengths of 594, 563, 522 and 475 nm indicating that there is no shift in the wavelengths of maximum absorption due to mixing although the intensity of each band appears diminished due to the overlap of the other bands from the different sized particles. Figure 17 presents the UV-vis absorbance spectra of four different nanoparticle fractions (dispersions in hexane) that were obtained after performing the CO_2 expanded liquid size separation process on the original sample mixture along with four dotted lines corresponding to the wavelengths of maximum absorption of 594, 557, 516, and 467 nm. There is little variation between the wavelengths of maximum absorption before and after the size separation process coupled with a corresponding increase in the intensity of the respective absorption bands for each particle size compared to the original sample mixture, thereby indicating that this CO_2 expanded liquid size separation process is very effective in separating CdSe/ZnS nanoparticles by size into four different colored fractions. Table 4 shows a comparison of the UV- vis wavelengths of maximum absorption for the four fractions both before and after the CO_2 expanded liquid nanoparticle size separation process.

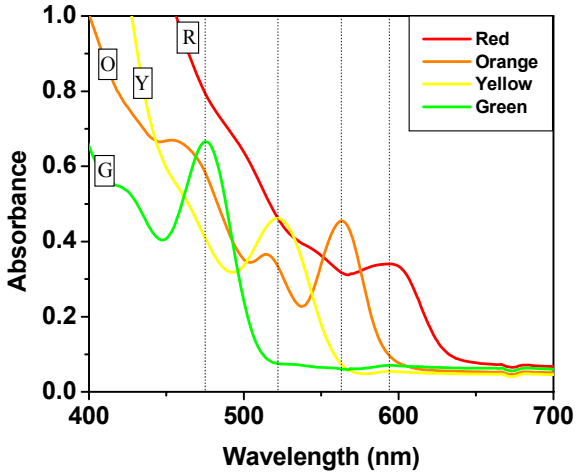

Figure 15. UV-visible absorbance spectra of CdSe/ZnS core shell nanoparticles capped with TOPO and dispersed in hexane (the as obtained nanoparticles from Evident Technology were dispersed in toluene and a solvent exchange was performed as described within to change the solvent medium to hexane). The spectra were normalized to give zero absorbance at 800 nm wavelength. Four dotted lines were drawn corresponding to the wavelength of the maximum absorption for the four different sized CdSe/ZnS nanoparticle dispersions.

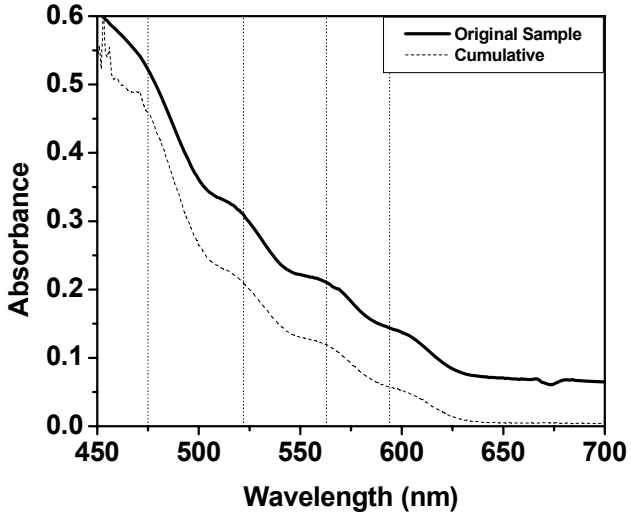

Figure 16. UV-visible absorbance spectra of a mixture of CdSe/ZnS core shell nanoparticles capped with TOPO and dispersed in hexane. The solid line spectrum was obtained by recording the UV-vis absorbance spectrum of the original mixture. The dashed line spectrum (cumulative spectrum) was obtained by adding the absorbances of the spectra of four different sizes of CdSe/ZnS core shell nanoparticles. The spectra were normalized to give zero absorbance at 800 nm wavelength. Four dotted lines were drawn corresponding to the wavelength of the maximum absorbance for four different sized CdSe/ZnS nanoparticles. There is no shift in the wavelength of the maximum absorbance due to mixing of four different sized nanoparticles.

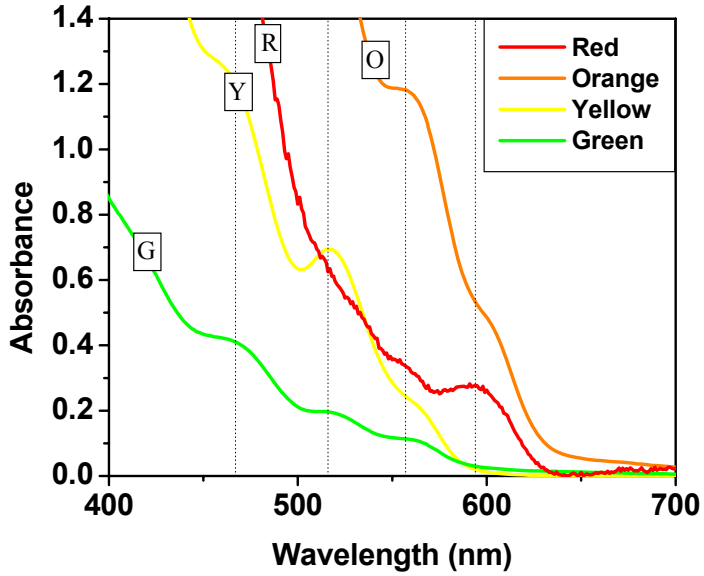

Figure 17. UV-visible absorbance spectra of CdSe/ZnS core shell nanoparticles obtained after the size separation of the original mixture in a spiral tube apparatus using CO_2 expanded liquid technique. These particles are capped with TOPO and dispersed in hexane. The spectra were normalized to give zero absorbance at 800 nm wavelength. Four dotted lines were drawn corresponding to the wavelength of the absorbance maximum for four different sized CdSe/ZnS nanoparticles. The wavelength of the maximum absorbance for the four different spectra obtained after the size separation are similar to the spectra obtained before the size separation process.

TEM Characterization. TEM grids were prepared for the original sample mixture (including all four sized CdSe/ZnS core shell quantum dots) as well as for each of the four individual nanoparticle fractions obtained after the size separation experiment. These grids were prepared by evaporative deposition by placing a small drop of the nanoparticle dispersion in hexane on a carbon coated copper TEM grid. These samples were examined using a Zeiss EM 10 Transmission Electron Microscopy (TEM) and the images obtained were further size analyzed using ImageJ software where each particle in the image was bounded by a rectangle and the diameter was estimated by the average of length and width of the rectangle. Figure 18 (A) shows an example of the STEM electron microscope images obtained from the original (unprocessed) sample comprised of a mixture of 4 different CdSe/ZnS dispersions with average crystal sizes ranging from 5.2 to 1.9 nm. The original sample mixture of four different sized CdSe/ZnS core shell quantum dots was size separated in the spiral tube using the pressure tunable properties of the CO_2 gas expanded liquid into 4 fractions. Figure 18 (B) presents example TEM images obtained from each of the four CdSe/ZnS fractions recovered after the CO_2 expanded liquid size separation process corresponding to the red dispersion (obtained between P = 0 psi and 660 psi), orange dispersion (obtained between P = 660 psi and 680 psi), yellow dispersion (obtained between P = 680 psi and 700 psi) and green dispersion (obtained between P = 700 psi and 800 psi). The different sized CdSe/ZnS nanoparticle fractions precipitated and adhered to the spiral tube surface according to these pressure changes and the translation of the liquid droplet location (via spiral tube rotation as described above) as illustrated in Figure 18(B) where the color of the recovered particle fraction changed from red, to orange, to yellow, to green with the increase in CO_2 pressure and droplet movement. After analyzing the TEM images of these fractions, it was observed that the average CdSe/ZnS particle size collected from the different locations decreased with the increase in CO_2 pressure as shown in Table 4. The average particle sizes of these four fractions obtained after the size separation process are very similar to the sizes of the original quantum dots obtained from Evident Technology prior to mixing. Both the UV-Vis spectral results and the particle sized obtained from the TEM images illustrate that CdSe/ZnS quantum dots can be rapidly (within 1 hour) separated by size using only hexane solvent and CO_2 as a anti-solvent in a CO_2 gas expanded liquid processing technique.

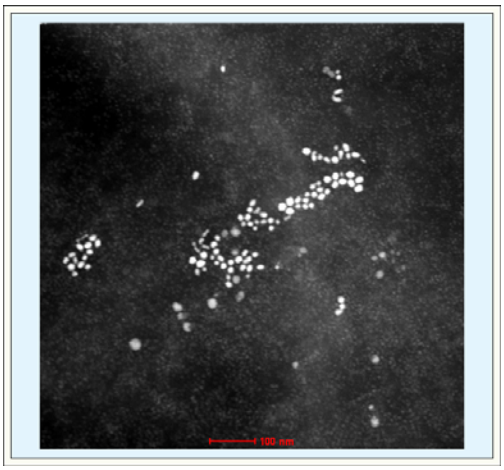

Figure 18A. Example STEM image obtained from the original (unprocessed) sample comprised of a mixture of 4 different CdSe/ZnS dispersions with average crystal sizes ranging from 5.2 to 1.9 nm.

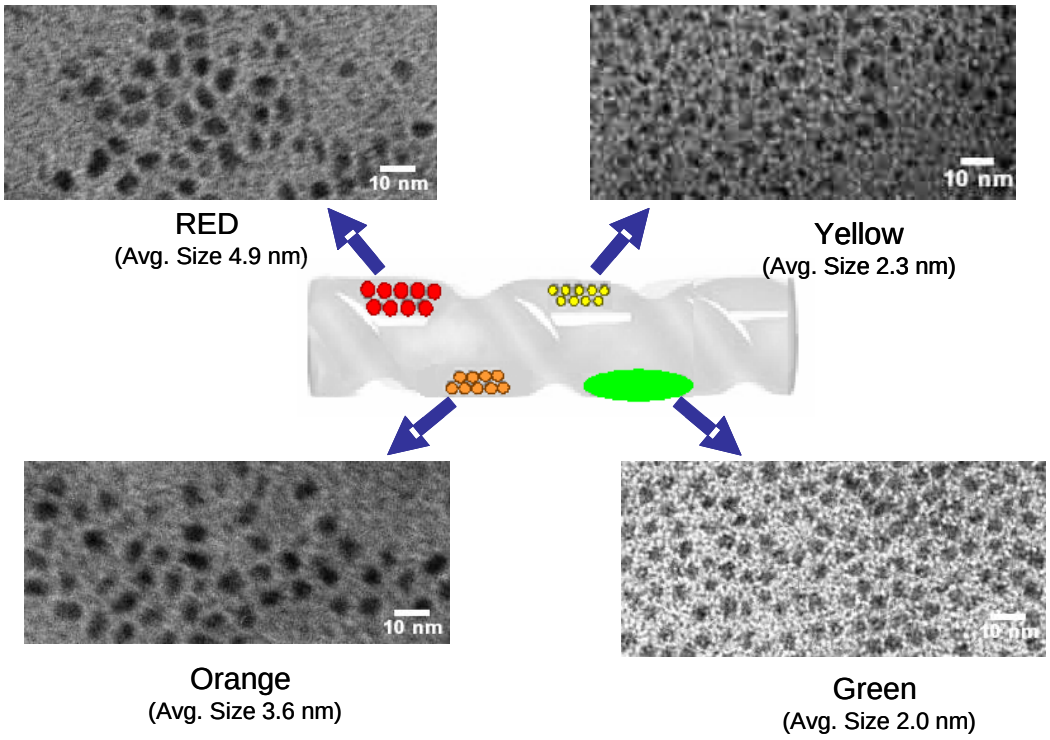

Figure 18B. Example TEM images obtained from each of the four CdSe/ZnS fractions recovered after the CO_2 expanded liquid size separation process using the high pressure spiral tube apparatus. The four images correspond to the particles obtained from the recovered red, orange, yellow and green dispersions, corresponding to average CdSe/ZnS crystal sizes of 4.9, 3.6, 2.3 and 2.0 respectively.

Fraction	UV- vis Wavelength (nm)		Mean Crystal Diameter (nm)		Pressure (Psi)	Std Dev (nm)	Particle Count
	Before Separation	After Separation	Before Separation	After Separation			
RED	594	594	5.2	4.9	0 to 660	1.6	356
Orange	563	557	3.2	3.6	660 to 680	1.3	322
Yellow	522	516	2.4	2.3	680 to 700	0.9	259
Green	475	467	1.9	2.0	700 to 800	0.8	379

Table 4. Comparison of the UV- vis wavelengths of maximum absorption and Statistical analysis of particle populations for the four fractions both before and after the CO_2 expanded liquid nanoparticle size separation process.

Thermodynamic analysis of the gas expanded liquid nanoparticle size separation process

In the current study, a thermodynamic model and related equations were developed including the derivation of the Hamaker constant and osmotic repulsive energy terms for binary mixtures of solvents interacting with a ligand tail. Appendix A provides our derivation of the Hamaker constant and the osmotic repulsive energy term for a mixture of solvents and one polymer (i.e. ligand tails). This was performed to improve our understanding of the size selective fractionation of ligand stabilized nanoparticles using a CO_2 gas expanded liquid precipitation process. This size selective precipitation process is based on controlled reduction of the solvent strength of the organic solution through increases in the antisolvent CO_2 concentration via pressurization. A decrease in the solvent strength

reduces the repulsive Osmotic contributions to the total interaction energy of the dispersion by weakening the interactions between the solvent and the ligand tails. Eventually, these repulsive forces in the dispersion are lowered to the point where they can no longer overcome the van der Waals forces of attraction between particles, thereby causing the particles to precipitate. This results in an ability to tune the size of the nanoparticles that are dispersed or precipitated simply by adjusting the CO_2 pressure. In this chapter, Osmotic energy and Hamaker constant expressions were developed for CO_2 gas expanded solvent mixtures consisting of an organic solvent (e.g. hexane) and antisolvent (e.g. CO_2). These expressions, coupled with appropriate thermodynamic data, were used to estimate the maximum size of dodecanethiol capped Ag nanoparticles that could be dispersed at a given CO_2 pressure by equating the total interaction energy to the Boltzman threshold stabilization energy (-3/2 k_BT). A parameter sensitivity analysis was performed to determine which parameters most affect the predicted maximum particle size that could be dispersed at a given CO_2 pressure. It was found that the length of the ligand tail that interacts with the solvent medium had the most influence on these total interaction energy calculations. Assuming complete solvation of the entire ligand tail, the model always overpredicted the size of the particles that would be precipitated at a given CO_2 pressure compared to the experimental results. Consequently, we have proposed that the entire length of the dodecane chain is not accessible to the solvent medium. As such, three phenomenological model variations were developed that provide for differing abilities of the ligand tails to interact with the solvent including an Extended Ligand Length Solvation Model, a Condensed Phase Model, and a Limited Ligand Length Solvation Model with the best fit of the experimental size separation data coming from the Limited Ligand Length Solvation Model. Equations for a surface fraction model based on UNIQUAC parameters and its viability for this process is also discussed.

Carbon dioxide gas expanded liquids have received a great deal of attention in various applications such as adjustable solvents for separations, in gas antisolvent crystallization, precipitation, organic and polymer microparticle formation as well as in tuning chemical reactions. These gas expanded liquids have garnered attention such that Jessop and Subramanium[16] have recently written a thorough review on gas expanded liquids and Eckert et. al.[15] have written a detailed review on the applications of tunable solvents in sustainable technology. The main advantage of this solvent system lies in the ability to tune solubility as well as other physicochemical properties. Another distinct advantage involves the easy removal of the CO_2 gas from the solvent mixture by depressurizing the system thereby allowing complete recycle of both the gas and the liquid constituents.

Over the last several years there has been ongoing research in the developing area of processing nanoparticles and other nanomaterials in CO_2 gas expanded liquids in order to take advantage of their unique properties. Our group has used the highly tunable solvent properties of CO_2 gas expanded liquids to vary the solvent strength of nanoparticle dispersions thus resulting in precipitation and deposition of particles by using CO_2 as an antisolvent.[17,18] Han and coworkers have also used CO_2 as an antisolvent in gas expanded liquids to precipitate ZnS nanoparticles from AOT reverse micelles in liquid isooctane. [19]

As described in previous chapters, we have used CO_2 as an antisolvent to size selectively precipitate and separate ligand stabilized metal nanoparticle dispersions into narrow distributions through fine adjustments in CO_2 pressure.[20-22] The dodecanethiol thiol capped polydisperse populations of silver (Ag) nanoparticles in hexane, with a mean diameter of 5.5 nm and a standard deviation of 31.9%, were size separated and fractionated into monodisperse size fractions by finely tuning the solvent strength of the CO_2 gas expanded alkane solvent mixtures by simply adjusting the applied CO_2 pressure. The organic solution expands upon increasing pressurization with CO_2 gas due to the condensation and miscibility of CO_2 with the organic solvent. CO_2 acts as an antisolvent for the non-polar ligands and thus its addition to the organic solution allows gradual size selective precipitation of the nanoparticles with simple adjustments in CO_2 pressure. Particle dispersability in a

solvent requires a sufficient solvent-ligand interaction in order to provide enough osmotic repulsive force to overcome the van der Waals forces of attraction between the particles in solution. Hence the degree of solvent-ligand interaction is diminished upon the gradual addition of CO_2 antisolvent through pressurization and since the larger particles in solution have greater van der Waals forces of attraction, the larger particles begin precipitating first upon worsening solvent conditions. Therefore, the particle dispersability and precipitation can be easily controlled by simply tuning the applied CO_2 pressure, which results in precise and controlled particle size separation and fractionation. In this quarter, a thermodynamic model was developed to analyze the experimental results.

Theoretical Section

A theoretical model based on total interaction energy was developed for the size selective fractionation process using the thermodynamic properties of CO_2 gas expanded liquids to predict the maximum particle size that can be dispersed as a function of CO_2 pressure (particles smaller than this maximum size will disperse and those larger than this maximum size will precipitate). Previously, studies have been done to predict the particle size that can be stabilized at given conditions in conventional liquid solvents[23], supercritical ethane[24], compressed propane[25] and supercritical CO_2[26]. Shah et al. [24] initiated this soft sphere modeling approach, where stabilization of nanoparticles in a given solvent depends on the balance between the van der Waals attractive forces with steric repulsive forces. Shah et al.[24] and Kitchens et. al.[23] have employed a total interaction energy model to correlate the solvent-ligand interaction with the maximum size of a ligand stabilized nanoparticle that can be dispersed within a given solvent system. Unfortunately, the maximum particle sizes predicted through this model are larger than the particle sizes obtained through experimental studies. The total interaction energy is the sum of attractive and repulsive terms as shown in equation (1) and depends on particle size, distance between the particles, ligand length, ligand composition and its density as well as solvent parameters. The van der Waals attractive force[27], Φ_{vdW}, between two particles increases with an increase in particle radius R or with a decrease in center to center separation distance between the particles d. Φ_{vdW} is directly proportional to the Hamaker constant, A_{131}. A_{131} is a proportionality factor that accounts for the interaction between two nanoparticles of the same material (component 1) across a solvent (component 3) and depends on A_{11} and A_{33}, where A_{11} is a constant value for metallic nanoparticles with A_{11} = 2.185 eV for silver[26] and A_{33} for the solvent is calculated by an equation of state based on Lifshitz theory[28]. A_{33} depends on the refractive index n, and dielectric constant ε of the solvent as given in equation (4) where k_B is Boltzmann's constant, h is Plancks's constant, v_e is the main electronic UV absorption frequency, generally assumed to be $3x10^{15}$ s^{-1} and T is temperature. Values of the refractive index and dielectric constant for CO_2[29] and organic solvents[30,31] at 25°C are given in Table 1 and values of n_{vacuum} and ε_{vacuum} are taken as 1.

$$\Phi_{total} = \Phi_{vdW} + \Phi_{osm} + \Phi_{elas} \tag{1}$$

$$\Phi_{vdW} = -\frac{A_{131}}{6}\left[\frac{2R^2}{d^2-4R^2} + \frac{2R^2}{d^2} + \ln\left(\frac{d^2-4R^2}{d^2}\right)\right] \tag{2}$$

$$A_{131} \approx \left(\sqrt{A_{11}} - \sqrt{A_{33}}\right)^2 \tag{3}$$

$$A_{33} = \frac{3}{4}k_B T\left(\frac{\varepsilon_3 - \varepsilon_{vacuum}}{\varepsilon_3 + \varepsilon_{vacuum}}\right)^2 + \frac{3h\nu_e}{16\sqrt{2}}\frac{\left(n_3^2 - n_{vacuum}^2\right)^2}{\left(n_3^2 + n_{vacuum}^2\right)^{3/2}} \tag{4}$$

The above expression (equation 3) for A_{131} applies to a binary system with one solvent (component 3) and one nanoparticle material (component 1). But, gas expanded liquids are mixtures of two solvent

components (in this case, CO_2 and hexane), so a new mathematical expression was developed to calculate the Hamaker constant where 3' represents one of the solvent components (in this case CO_2) and 3" represents the other solvent component (e.g. hexane). In equation (5), $\tilde{\phi}_{3'}$ is the CO_2 volume fraction in the solvent mixture excluding the ligand, and $A_{(33)'}$ is the Hamaker constant for CO_2. Similarly, $\tilde{\phi}_{3"}$ is the volume fraction of hexane in the solvent mixture excluding the ligand, and $A_{(33)"}$ is the Hamaker constant for hexane. The complete derivation of the equation (5) is given in supporting information.

$$A_{131} \approx \left[\sqrt{A_{11}} - \left(\tilde{\phi}_{3'}\sqrt{A_{(33)'}} + \tilde{\phi}_{3"}\sqrt{A_{(33)"}}\right)\right]^2 \tag{5}$$

For the repulsive contribution, Vincent et. al.[32] proposed the osmotic and elastic repulsive terms where the osmotic term is related to the solvation of the ligand tails between the colliding nanoparticles. The osmotic term depends on the free energy of the solvent-ligand tail interactions. On the other hand, the elastic term results from the entropy loss due to the compression of ligand tails present between two metal cores. Shah et. al.[24] introduced these two repulsive terms, originating from "soft sphere" theory, to the total interaction energy to balance the van der Waals forces of attraction between nanoparticles. These repulsive contributions, as given in equation (6-8), depend largely on the ligand length and solvent parameters as well as on the particle radius, R, and center to center particle distance, d. v_{solv} is the molar volume of the solvent and Avogadro's number (N_{av}) was used to convert this into molecular volume of the solvent. h is the separation distance from the particle surfaces calculated using equation (9). The elastic term, given by equation (8), depends on the ligand density (ρ) and its molecular weight (MW_2).

$$\Phi_{osm} = \frac{4\pi R k_B T}{(v_{solv}/N_{av})}\phi^2\left(\frac{1}{2}-\chi\right)\left(l-\frac{h}{2}\right)^2 \qquad l<h<2l \tag{6}$$

$$\Phi_{osm} = \frac{4\pi R k_B T}{(v_{solv}/N_{av})}\phi^2\left(\frac{1}{2}-\chi\right)\left[l^2\left(\frac{h}{2l}-\frac{1}{4}-\ln\left(\frac{h}{l}\right)\right)\right] \qquad h<l \tag{7}$$

$$\Phi_{elas} = \frac{2\pi R k_B T l^2 \phi\rho}{MW_2}\left\{\frac{h}{l}\ln\left[\frac{h}{l}\left(\frac{3-h/l}{2}\right)^2\right] - 6\ln\left(\frac{3-h/l}{2}\right) + 3\left(1-\frac{h}{l}\right)\right\} \qquad h<l \tag{8}$$

$$h = d - 2R \tag{9}$$

χ is the Flory-Huggins interaction parameter in the osmotic repulsion term and is a function of the Hilderbrand solubility parameter of the solvent (component 3) and ligand (component 2), as given in equation (10), where v_3 is the molar volume of the solvent and R is the ideal gas constant.

$$\chi_{32} = \frac{v_3}{RT}\left(\delta_3 - \delta_2\right)^2 \tag{10}$$

This osmotic repulsive term given above applies to one solvent (component 3) interacting with the ligand tails but in the case of the two solvents in the gas expanded liquid, a new mathematical expression was developed as given in the equation below. The complete derivation of the osmotic repulsive energy term for several solvent components interacting with the ligand tails is given in the supporting information.

$$\Phi_{osm} = \frac{4\pi R k_B T}{(v_M / N_{av})} \phi^2 \left[x_{3'} \left(\frac{1}{2} + \tilde{\phi}_{3''} r_{3'} \chi_{(3'3'')} - r_{3'} \chi_{(3'2)} \right) + x_{3''} \left(\frac{1}{2} - r_{3''} \chi_{(3''2)} \right) \right] \left(l - \frac{h}{2} \right)^2$$

When $l < h < 2l$ (11)

$$\Phi_{osm} = \frac{4\pi R k_B T}{(v_M / N_{av})} \phi^2 \left[x_{3'} \left(\frac{1}{2} + \tilde{\phi}_{3''} r_{3'} \chi_{(3'3'')} - r_{3'} \chi_{(3'2)} \right) + x_{3''} \left(\frac{1}{2} - r_{3''} \chi_{(3''2)} \right) \right] \left[l^2 \left(\frac{h}{2l} - \frac{1}{4} - \ln\left(\frac{h}{l} \right) \right) \right]$$

When $h < l$ (12)

Where *3'* represents one of the solvent components (in this case, CO_2) and *3"* represents the other solvent component (e.g. hexane), and v_M in this case represents the molar volume of the solvent mixture of CO_2 and hexane excluding the ligand.

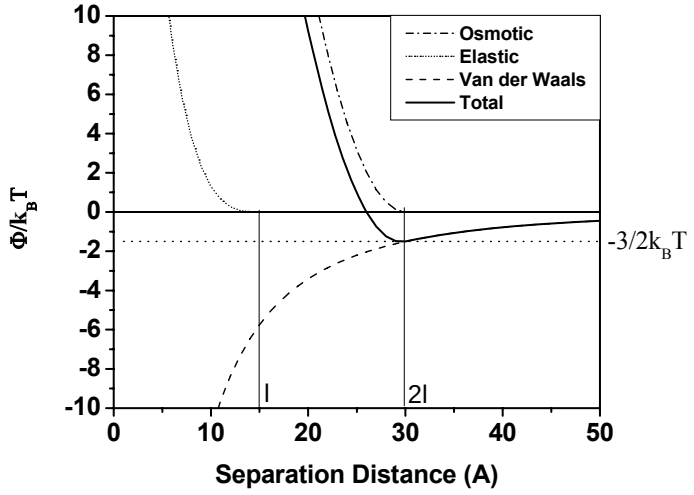

Figure 19. Representation of the attractive (van der Waals) and repulsive forces (osmotic and elastic) contributing to the total interaction energy for 12.6 nm dodecanethiol coated silver nanoparticles dispersed in CO_2 gas expanded hexane at a CO_2 pressure of 500 psi and system temperature 25°C.

As can be seen from these equations and from Figure 19, the repulsive energies do not contribute to the total interaction energy until the separation distance is less than twice the ligand length *l*. $r_{3'}$ and $r_{3''}$ are the segment lengths of molecules of CO_2 and hexane and their values are assumed to be $r_{3'} = 1$ and $r_{3''} = v_{3''} / v_{3'}$, respectively. $x_{3'}$ and $x_{3''}$ are mole fractions of CO_2 and hexane, respectively, in the solvent mixture of CO_2 and hexane excluding the ligand, as given in Table 5, where molar compositions and molar volumes of the liquid phase for CO_2 gas expanded hexane at 25°C were calculated using the Peng-Robinson Equation of State with the binary interaction parameter set as 0.125 ($k_{12} = 0.125$ for CO_2 and hexane). $\tilde{\phi}_{3''}$ is the volume fraction of hexane in the CO_2 and hexane solvent mixture excluding the ligand. ϕ is the ligand volume fraction within the volumetric shell of one extended ligand length from the particle surface (i.e. local volume fraction of the ligand coating the particle surface), and it was calculated by modeling the ligand as a cylindrical structure extending from the particle surface. It is given in the literature that the ligand surface coverage varies with particle size from 30% for small nanocrystals (< 4 nm) to 60% for nanoparticles with a larger size range.[33] It was measured by Korgel et al.[33] that thiols have a surface coverage of 75% on silver

nanoparticle surfaces for particles of 4 to 7 nm in size.[34] The following expression for ligand volume fraction assumes a surface coverage of 75%.

$$\phi = 0.75\left(\frac{3R^2 l}{(R+l)^3 - R^3}\right) \tag{13}$$

Compound	v_L (cm³/mol)	δ (J/cm³)^1/2	Dielectric Constant (ε)	Refractive Index (n)
CO_2	55	12.3	1.483	1.185
Hexane	132	14.9	1.882	1.372
Pentane	116	14.5	1.836	1.355
Heptane	147	15.2	1.917	1.385
Octane	164	15.3	1.942	1.393

Table 5. Physical properties of various solvents. The values for hexane and CO_2 were used to model the size fractionation process of dodecanethiol stabilized silver nanoparticles using CO_2 gas expanded liquids at 25°C.

Total Interaction Energy Calculations

All of the forces which contribute to the total interaction energy were calculated for CO_2 gas expanded hexane at various pressures below the CO_2 vapor pressure (860 psi). As an example, the contributions of these forces are shown in Figure 19 as a function of the separation distance, *h*, at a CO_2 pressure of 500 psi. Also shown in Figure 19 is a dotted line, drawn at -3/2 k_BT, that represents the minimum threshold energy for Brownian motion necessary to disperse the particles of a given size within the bulk solvent. The total interaction energy for a given particle size should be above this minimum threshold energy at the given conditions in order to stabilize the particles. Due to van der Waals forces of attraction, particles approach each other, and if not sufficiently solvated and stabilized in the medium, they will flocculate and precipitate. If particles are larger than a threshold size, the minima in the total interaction energy curve for those sized particles drops below -3/2 k_BT and those particle will precipitate from solution. The sum of the elastic and repulsive forces thereby counteracts these van der Waals forces of attraction and result in an increase in particle dispersibility. The elastic term, which is due to tail-tail interactions, depends on thiol density and its volume fraction. It has a very small contribution to the total interaction energy except at very close separation distances. On the other hand, the osmotic force strongly counteracts the van der Waals forces of attraction and depends on the solvent molar volume, ligand length, ligand volume fraction and solvent-ligand interaction (given as χ in this model). Stabilized particles can therefore be induced to precipitate with the addition of an antisolvent, thereby decreasing the solvent strength and reducing the solvent-ligand interaction below the value necessary to disperse a given sized particle. In the example shown in Figure 19, the maximum size of the particles that can be stabilized at these conditions can be obtained by equating the total interaction energy with the Boltzmann threshold stabilization energy (-3/2 k_BT). To improve the CO_2 gas expanded liquid nanoparticle precipitation process, it would be important to be able to predict the threshold particle size where particles larger than this threshold size are precipitated and particles smaller than this threshold size are dispersed at a given set of conditions. In this study, threshold particle size for precipitation/dispersion has been calculated at various operating conditions in the CO_2 gas expanded mixtures. In the example in Figure 19, a hexane/CO_2 mixture with a CO_2 pressure of 500 psi results in a threshold size of 12.6 nm for dodecanethiol stabilized silver nanoparticle. This model helps in finding the threshold nanoparticle size which can be

precipitated/dispersed at various conditions as a function of the solvent, ligand, temperature and antisolvent CO_2 pressure.

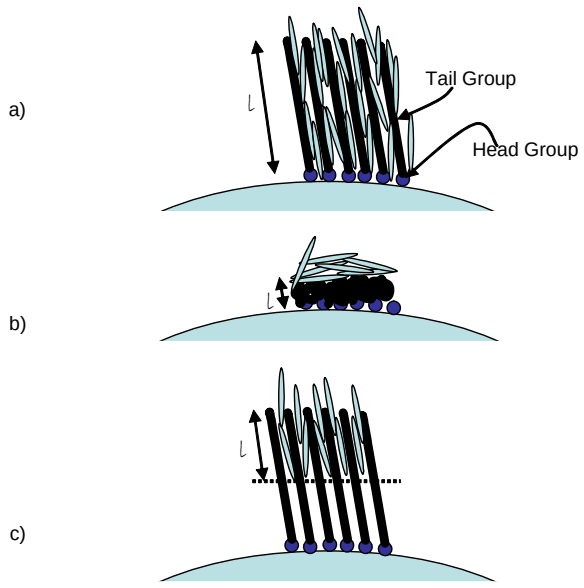

Figure 20 Schematic of three phenomenological models used to estimate the threshold particle size for precipitation/dispersion in CO_2 expanded size separation process. In the Extended Ligand Length Solvation Model (ELLSM), the ligand tails are extended completely and the whole length of the ligand alkyl tail interacts with the solvent. In the Condensed Phase Model (CPM), the ligand tails are condensed and effective ligand lengths were calculated by assuming the volume fraction as unity. In Limited Ligand Length Solvation Model (LLLSM), effective ligand lengths available for interaction with solvent were determined by matching the model predicted particle size to the size obtained from the size fractionation experiments at a given set of conditions using the ligand length as an adjustable parameter.

We have considered three basic phenomenological variations on this total interaction energy model based on the nature of the interaction between the ligand tails and the solvent. A schematic of these three models is given in Figure 20 that illustrates the ligand tail arrangement and position within the solvent environment to depict differences in tail solvation and ligand length accessibility by the solvent. In the Extended Ligand Length Solvation Model (ELLSM), ligand tails are considered to be fully extended and the entire length of the thiol's alkyl tail is available to interact with the solvent. In the Condensed Phase Model (CPM), the ligand tails are considered to be condensed on the particle surface due to poor solvent strength and effective ligand lengths available for solvation were calculated by assuming the ligand volume fraction as unity. In Limited Ligand Length Solvation Model (LLLSM), effective ligand lengths available for interaction with solvent were determined by matching the model predicted particle size to the size obtained from the size fractionation experiments at a given set of conditions using the ligand length as an adjustable parameter. Hence effective ligand lengths were fit to the experimental data.

Pressure (Psi)	Volume Fraction		Mole Fraction		Molar Volume (cm^3/mol)
	Hexane	CO_2	Hexane	CO_2	
0	1	0	1	0	131
500	0.732	0.268	0.529	0.471	88
550	0.670	0.330	0.460	0.540	84
600	0.634	0.366	0.416	0.584	79
625	0.600	0.400	0.380	0.620	76
650	0.560	0.440	0.350	0.650	74
700	0.468	0.532	0.265	0.735	68

Table 6. Compositions and Molar volumes of the liquid phase for CO_2 gas expanded hexane at 25°C calculated using the Peng-Robinson Equation of State with the k_{12} binary interaction parameter set as 0.125 (k_{12} = 0.125 for CO_2 and Hexane).

Experimental Section		Theoretical Section			
Pressure Range (Psi)	Mean Diameter (nm)	Pressure (Psi)	Threshold Particle Diameter (nm)		
			ELLSM	CPM	LLLSM
0 - 500	6.7	500	12.6	6.7	6.7
500 - 550	6.6	550	12.5	6.6	6.6
550 - 600	5.8	600	12.4	5.8	5.8
600 - 625	5.3	625	12.3	5.3	5.3
625 - 650	4.8	650	12.2	4.8	4.8
650 - 700	4.1	700	12.0	4.1	4.1

Table 7. Comparison of experimental Ag particle diameters obtained at different pressures in the CO_2 gas expanded liquid particle size separation process and predicted particle diameters using three models based on total interaction energy. The experimental section shows the mean diameter of dodecanethiol-coated silver particles precipitated within the corresponding CO_2 pressure ranges. The theoretical section provides predictions of the threshold particle diameter that can be precipitated/dispersed using three phenomenological variations of the total interaction energy model based on a soft sphere approach. In the Extended Ligand Length Solvation Model (ELLSM), ligand tails are extended completely and the whole length of thiol molecule interacts with the solvent. In the Condensed Phase Model (CPM), ligand lengths are condensed on the particle surface and are calculated by assuming the volume fraction as unity. In the Limited Ligand Length Solvation Model (LLLSM), only a part of entire ligand length is solvated and is calculated by matching the predicted particle size with the size obtained from size fractionation experiments.

Extended Ligand Length Solvation Model (ELLSM)

In this model, it was assumed that the whole alkyl ligand tail is extended from the particle surface and solvated by the solvent as shown in Figure 20(a). The threshold particle size which can be precipitated/dispersed at a set of given solvent conditions was calculated by balancing the total interaction energy with the Boltzmann threshold stabilization energy (-3/2 k_BT) by considering that the entire ligand length (dodecane length 15 Å) interacts with the solvent. Similarly, threshold particle sizes were calculated at various CO_2 pressures that correspond to conditions used in the CO_2 expanded hexane particle precipitation experiments. Comparing the calculated threshold particle sizes to the experimental results, these calculated threshold particle sizes are always much larger than experimental and there was not much change in the calculated particle size with the corresponding changes in the CO_2 pressure as shown in Figure 22. Unfortunately, the ELLSM model is unable to predict both the threshold size and the effect of pressure on this threshold size. To improve these calculations it is important to understand which parameters have the greatest influence on the

stabilization threshold size and the effect of CO_2 pressure on this size as measured experimentally. As such, we performed a sensitivity analysis on various parameters to understand which variables most affect these modeling results.

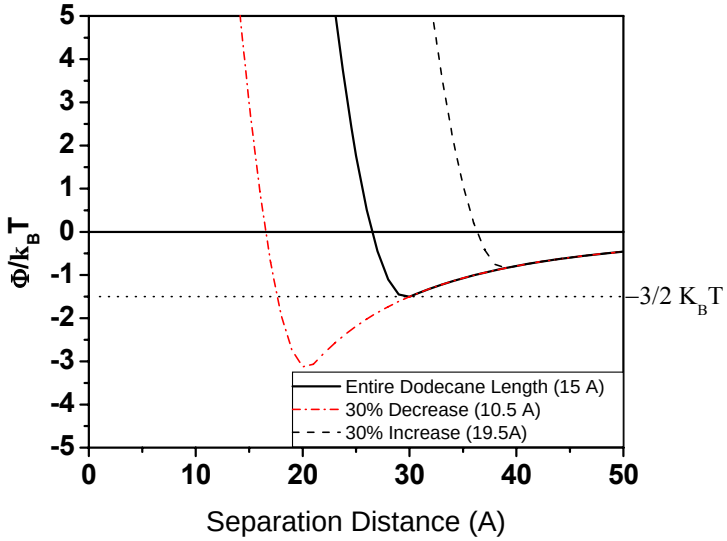

Figure 21. Demonstration of the effect of the degree of ligand solvation on the total interaction energy with a 30% increase and 30% decrease in the effective dodecanethiol ligand length

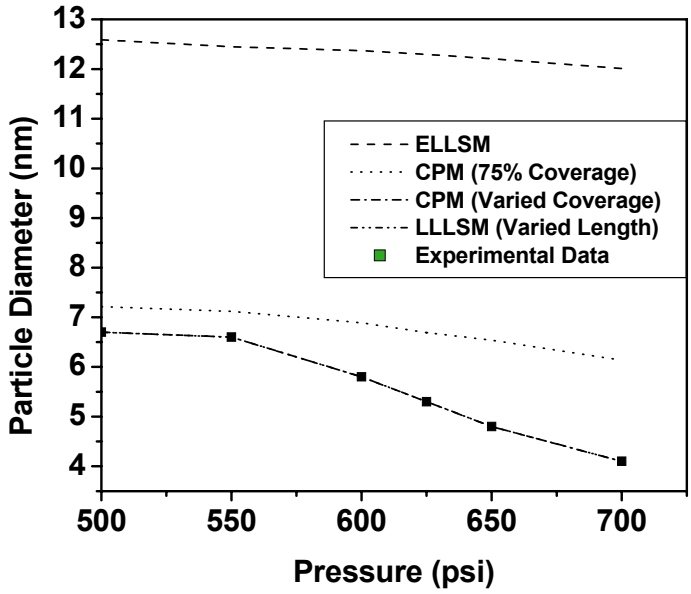

Figure 22. Comparison of Ag particle diameters precipitated in CO_2 gas expanded hexane experiments and threshold particle diameters predicted using the Extended Ligand Length Solvation Model (ELLSM), the Condensed Phase Model (CPM), and the Limited Ligand Length Solvation Model (LLLSM) as a function of CO_2 pressure. The experimental results are presented for dodecanethiol coated silver particles precipitated from hexane/CO_2 mixtures.

Parameter	Base Parameter Values Used	Threshold Particle Diameter (nm)	
		30% increase	30% decrease
Carbon Dioxide			
Dielectric Constant	1.483	12.6	12.6
Refractive Index	1.185	14.1	12.6
Solubility Parameter $(J/cm^3)^{1/2}$	12.3	12.6	12.6
Molar Volume (cm^3/mol)	55	12.4	12.9
Other Parameters			
Hamaker Constant (eV)	2.185	10.7	16.2
Surface Coverage	75%	12.6	12.5
Mixture Volume (cm^3/mol)	87	12.6	12.6
Length Of Ligand (Å)	15	16.4	8.8

Table 8. Results of sensitivity analysis performed at CO_2 pressure of 500 psi for analysis of the parameters affecting the threshold particle size obtained from the Extended Ligand Length Solvation Model. A 12.6 nm threshold size is obtained using the base parameter values of 500 psi CO_2 pressure. This table shows the change in the predicted threshold particle size using a 30% increase and a 30% decrease in various parameters relative to the threshold particle size obtained using the base values of the parameters.

Parameter Sensitivity Analysis

The physicochemical properties of CO_2 gas expanded liquids are difficult to determine because the CO_2 in the liquid hexane/CO_2 mixture behaves as a hypothetical liquid despite the fact that the system pressure is below its vapor pressure, making it different to determine pure component CO_2 "liquid" properties at these operating conditions. Liquid volumes and solubility parameters for CO_2 as a solute in hexane mixtures were obtained from the reports in the literature. Given the nonideality of these CO_2 expanded hexane mixtures, and the uncertainty of thermodynamic mixing rules in this case, sensitivity analysis was performed on these literature obtained CO_2 properties in order to determine the impact of potential measurement errors on these predicted threshold particle sizes. Sensitivity analysis was performed to analyze the effects of these properties of CO_2 as well as the influence of other model parameters such as ligand length solvation, surface coverage of the ligands on the particle surface, solvent mixture volume and the Hamaker constant of the metallic Ag particles on the over predicted threshold particle size. Sensitivity analysis was performed on the property values of the hypothetical liquid CO_2 and the other model parameters by increasing or decreasing the parameters by 30% from the baseline parameter values in order to determine the variation in the threshold particle size obtained. Note that, at CO_2 pressure of 500 psi using the ELLSM model the base parameter values yielded a threshold size of 12.6 nm, and the sensitivity to these parameters is determined by comparing the increased and decreased values to this base case of 12.6 nm. Also note that the experimental particle size at these conditions is 6.7 nm. As indicated above, the ELLSM model predicted a threshold particle size at the base conditions of 12.6 nm compared to this experimentally obtained size of 6.7 nm. The sensitivity analysis on the model parameters will allow us to determine which parameters most influence particle dispersability.

Van der Waals forces depend on the refractive index and dielectric constant of CO_2 as well as the Hamaker constant of the silver metal surface. The value of the CO_2 dielectric constant used in the ELLSM model was 1.483. With a 30% increase (1.928) or 30% decrease (1.038) in this base value of CO_2 dielectric constant, there was not a significant change in the threshold particle diameter from the 12.6 nm value obtained at the base parameter values as shown in Table 8. On the other hand, a 30%

increase (1.54) in the CO_2 refractive index from its base value (1.185) results in a large increase in particle size (12.6 nm to 14.1 nm). However, a 30% decrease (0.829) in the CO_2 refractive index did not result in a large change in particle size. The base value of the Hamaker constant of the silver nanoparticle surface was taken as 2.185 eV. A 30% increase in the Hamaker constant value (2.84 eV) decreases the threshold particle size to 10.7 nm while a 30% decrease in the Hamaker value (1.53 eV) increases the particle size to 16.2 nm. While this increase in the Hamaker constant does reduce the predicted threshold size (10.7 nm) towards the experimental result (6.7 nm), Eichenlaub et al.[35] have shown that the Hamaker constant for Ag-Ag interaction cannot be more than 3.12 eV (a maximum value reported), which results in a threshold size of 10.1 nm. It should be noted that Eichenlaub et al. [35] reported a range of possible Hamaker constant values for Ag ranging from 1.02 eV to 3.12 eV with an average value of similar to the value of 2.185 eV[24] used in this study.

Osmotic forces depend on the solubility parameters of the solvent components as well as the ligand, solubility parameter, the ligand length and the ligand surface coverage as well as the solvent volumes. The properties of the pure hexane and pure ligand alkyl tail are well known in the literature and we are not investigating in the parameter sensitivity analysis. As shown in Table 8, among all the parameters investigated the ligand length (actual value = 15 Å) has the greatest influence on the threshold particle size, where the particle size increased to 16.4 nm from 12.6 nm with a 30% increase (19.5 Å) in the ligand length. The threshold particle size was also changed to 8.8 nm from 12.6 nm with a 30% decrease (10.5 Å) in the ligand length. It is reasonable, based on discussions below, that the entire ligand length would not be available for complete solvation by the solvent medium. Therefore, the effective ligand length in the model could be decreased more than the 30% used in this sensitivity analysis in order to finely tune the threshold particle size to match the experimental obtained results. The effect of the degree of ligand solvation accounted for in the model by adjusting the "effective" ligand length is more clearly demonstrated in Figure 21 which shows the total interaction energy for three different ligand lengths (15, 19.5, 10.5 Å). Due to this sensitivity analysis, we find that the ligand length has the most pronounced affect on the threshold particle size predicted in the ELLSM. As such, we have developed two other variations of this model to explain our experimental results based on differing degrees of tail solvation and "effective" ligand lengths for this solvation.

Condensed/Collapsed Phase Model (CPM)

After performing the sensitivity analysis, it was observed that ligand length is the variable that has the most impact on the threshold particle size predicted in the ELLSM model. Indeed, the degree to which the solvent has access to the ligand tail length decides the magnitude of the ligand-solvent interaction and hence the effective ligand length being solvated impacts the repulsive energy. We considered two variations of the model based on different ligand lengths being able to interact with the solvent base on physical phenomena constraints.

De Gennes [36-38] has shown that for a poor solvent, a polymer chain interacts more with itself than with the solvent and makes knots on itself. In other words, the polymers repel each other and extend more in a good solvent (interact more with the solvent) whereas the polymer collapses and condenses in a poor solvent. For example, In one of De Gennes articles[36], it was shown that the polymer coil diameter is proportional to the polymerization index raised to a ½ power in poor solvent compared to a $\frac{3}{5}$ power in good solvent. In the current study, the addition of antisolvent CO_2 decreases the solvent strength of the solvent mixture thereby reducing the ligand length interacting with the now poorer solvent. As an alternative to the ELLSM model, we have considered the scenario where the solvent strength would be low enough that the ligand tails are completely condensed on the particle surface. Figure 20 (b) shows the condensed phase arrangement of thiol tails with a ligand volume fraction considered to be unity. This model is referred to as the Condensed Phase Model (CPM) since it is

considered that all the thiol tails are collapsed and condensed. The effective ligand length which is available for interaction is thus calculated by setting the ligand volume fraction in equation (13) equal to 1 and solving for *l,* for a given particle diameter, R obtained experimentally. The value of the ligand length which was obtained was 8.8 Å for a 6.7 nm particle diameter. The effective ligand length has reduced from 15 Å (in ELLSM) to 8.8 Å (in CPM) for a 6.7 nm particle diameter. The effective ligand lengths at different CO_2 pressures were calculated by setting the ligand volume fraction in equation (13) to a value of 1 with a ligand surface coverage of 75% [34] for each experimental particle size obtained at a particular CO_2 pressure. At this point, all the calculations of the forces were performed with these new effective ligand lengths and the respective ligand solubility parameters that correspond to these alkyl tail lengths. The predicted threshold particle size obtained from the CPM model is much lower than the ELLSM model and closer to the experimental data as shown in Figure 22. Unfortunately, these results still slightly over predict the threshold particle diameters at the lowest pressure of 500 psi and do not demonstrate the significant effect of pressure on the threshold particle diameter as observed experimentally although a slight decrease in diameter is observed with increasing CO_2 pressure. While the CPM model does not capture the effect of CO_2 pressure compared to the experimental data, it does illustrate that limited tail solvation likely accounts for the differences in the ELLSM model and the experimental results.

In an effort to account for the difference between the threshold particle diameters obtained from the Condensed Phase Model (with constant surface coverage) and the experimental data, the degree of surface coverage, in the CPM model, was adjusted from the literature value of 75%.[34] These results for this CPM model with variable surface coverage model are shown in Table 5. These results again indicate that a small variation in surface coverage from 69.3% to 58.3% can account for the change in particle size precipitated at the various experiment pressures. These results again indicate that the degree of ligand tail solvation is the most important parameter for controlling particle dispersability. In this case the model was fit to the experimental data at each pressure by adjusting the surface coverage and determining the corresponding effective length according to equation (13). It has been shown in literature that ligand surface coverage does not remain constant for all particle sizes.[33] Ligand surface coverage on the gold particles was found to vary with particle size from 30% for small nanocrystals (< 4 nm) to 60% for nanoparticles with a larger size range. However, the ligand surface coverage measured by Korgel et. al. for dodecanethiol coated Ag particles in the range of 4 to 7 nm, is a constant value of 75%. One major concern with the CPM model involves the dichotomy of the concept of the ligand tails being completely condensed on the particle surface while also being able to interact with the solvent through tail solvation. There is experimental evidence that thiol tails on a metal surface are in the extended mode. For example, using IR spectroscopic and ellipsometric data, Porter et al.[39] have shown that thiol tails with hydrocarbon group ($-CH_2$) greater than 9 assemble on gold surfaces in a densely packed manner with fully extended alkyl chains tilted from the surface normal by 20-30^o. This suggests that the Condensed Phase Model may not be the correct phenomenological model for our experimental system.

	Condensed Phase Model (75% Surface Coverage)		Condensed Phase Model (Variable Surface Coverage)			Limited Ligand Length Solvation Model (75% Surface Coverage)	
Pressure (Psi)	Effective Ligand Length (Å)	Threshold Particle Size (nm)	Surface Coverage (%)	Effective Ligand Length (Å)	Threshold Particle Size (nm)	Effective Ligand Length (Å)	Threshold Particle Size (nm)
500	8.8	7.2	69.3	8.2	6.7	8.2	6.7
550	8.7	7.1	69.2	8.2	6.6	8.1	6.6
600	8.5	6.9	63.2	7.4	5.8	7.3	5.8
625	8.4	6.7	60.3	7.0	5.3	6.8	5.3
650	8.2	6.5	60.2	6.9	4.8	6.3	4.8
700	7.9	6.1	58.3	6.5	4.1	5.9	4.1

Table 9. Effective ligand lengths and threshold Ag particle sizes as a function of CO_2 pressure obtained from the Condensed Phase Model using 75% surface coverage, the Condensed Phase Model with surface coverage as an adjustable parameter, and the Limited Ligand Length Solvation Model.

Limited Ligand Length Solvation Model (LLLSM)

Another model which was considered is shown in Figure 20(c) where the ligand tails are fully extended yet the entire length is not accessible to the solvent, such that the effective ligand length which is interacting with the solvent is smaller than the total ligand length. This effective ligand length decreases with an increase in the antisolvent CO_2 concentration (pressure) due to the weaker solvent mixture being less able to solvate the ligand tails. In other words, the total ligand length is extended but only part of it is interacting with the solvent because only a portion of the ligand length is coming in contact with the solvent. As shown in Figure 20(c) if the ligand tails are densely packed (assume surface coverage 75%) then it would be very difficult for hexane solvent molecules, which are half the length of dodecanethiol ligand molecules, to penetrate the tortuous path between the ligand tails and solvate the entire ligand length. Effective ligand lengths were obtained by matching the threshold particle size predicted from the total interaction energy model with the experimental results at constant ligand surface coverage of 75%. Ligand Solubility parameters were also adjusted according to the effective alkyl tail length in this model. The results from this Limited Ligand Length Solvation Model are given in Table 9. The effective ligand length required to disperse a threshold particle size of 6.7 nm at a CO_2 pressure of 500 psi is 8.2 Å compared to the total length of the dodecanethiol ligand which is 15 Å. Similarly, effective ligand lengths were calculated at each of the antisolvent CO_2 pressures by fitting the threshold particle size from the model to our experimental data at each of these CO_2 pressures. Considering limited ligand length solvation, the total interaction energy model indicates that the effective ligand length of the dodecane alkyl tail which is available to the solvent decreases from 8.2 Å to 5.9 Å corresponding to the Ag particle sizes of 6.7 nm to 4.1 nm, and CO_2 pressures from 500 psi to 700 psi, respectively. These results indicate that changes in the effective ligand length, due to solvation changes, can account for both the dispersed particle size as well as the effect of CO_2 pressure.

Scaleup of the CO_2-Expanded Liquid Nanoparticle Fractionation Process

In order to show that this process could be commercially viable it is necessary to scale up the apparatus to be able to separate samples on the gram or larger scale. The new system consists of vertically mounted high pressure vessels (3 in series) where between each vessel is a needle valve to isolate the vessels from each other. Connected to the top of the vessel cascade is a pressure transducer as well as a valve to which a syringe pump is connected. We have developed the following processing

procedure. To begin a run, all the isolation valves between vessels need to be closed. The original nanoparticle dispersion (gold or silver nanoparticles dispersed in hexane or any suitable solvent) is placed in the top vessel and the system is sealed. Slowly, the top vessel is pressurized with carbon dioxide. As the pressure increases, the dispersion begins to expand as the CO_2 enters the liquid, thus reducing the solvent strength of the dispersion. Once the desired pressure is reached, the syringe pump is set to deliver constant pressure and the system is allowed to rest while the nanoparticles precipitate onto glass wool that will be placed in each vessel. After a settling time has passed, the needle valve between the top two vessels is opened slightly, enough to allow the dispersion to flow, via gravity, into the second vessel. As the dispersion slowly flows into the second vessel, the pressure in the top vessel will not change (due to increased volume) since the syringe pump will be set to deliver constant pressure the weaker solvent strength of the dispersion will be maintained. At the instant all of the dispersion has been transferred to the second vessel, the pressure will drop significantly since the effective volume of the system doubles. Normally this would be a problem; the lower pressure would lead to a decreased CO_2 concentration in the gas-expanded liquid which would lead to a stronger solvent strength causing the already precipitated particles to redisperse. However, since the dispersion has been moved from where the particles precipitated, this is not a problem. Once the dispersion has settled in the second vessel, the system is then pressurized to the next higher pressure corresponding to the size of particle to be precipitated. The process is then repeated for the desired number of fractions. Upon reaching the final fraction, the same procedure is followed, however, rather than passing the dispersion into an additional high pressure vessel, the dispersion is passed into an external (low pressure) collection vessel.

The last several months of this project involved the construction of the scaled up apparatus, preliminary safety tests, preliminary separation experiments, further apparatus refinements (the scaled up apparatus schematic can be seen in Figure 23), and the final separation experiments have been completed. From the experiments performed, it can be concluded that this apparatus and technique is capable of size-selectively separate large amounts of nanoparticles (i.e. samples > 20ml). After verifying that the equipment was sealed and able to withstand the necessary pressures, preliminary separation experiments were performed. As proof of concept experiments, small quantities of nanoparticle dispersions were used, on the order of 5 mL of a 1 mg / mL silver, dodecanethiol capped nanoparticle in hexane dispersion. From previous UV-VIS experiments, it is know that at a CO_2 pressure of 700 PSI, all particles precipitate from solution. With this in mind, we wanted to separate a particle dispersion into two fractions, one fraction of particles precipitated at 600 PSI and a second fraction of the smaller particles at 700 PSI. This would allow us to examine the effectiveness of the separation as well as to see if any precipitated particles were being washed from vessel to vessel due to the induced flow. This could be seen by a third fraction collected at the end of the experiment.

To begin the experiments, the nanoparticle dispersion was loaded into the first high pressure vessel and the system was sealed. The first vessel was pressurized to a CO_2 pressure of 600 PSI. The system was allowed to equilibrate and rest for 10 minutes, during which the largest particles precipitated out of solution and onto the walls of the vessel. The isolation valve between the first and second vessels was slowly opened while the syringe pump was set to maintain the pressure in the first vessel at 600 PSI. The greater pressure in the first vessel along with gravity induced flow of the nanoparticle dispersion into the second vessel. Once the remaining dispersion was completely in the second vessel, the first and second vessels were pressurized to a CO_2 pressure of 700 PSI in which the remaining particles precipitate out of the dispersion. This could be clearly seen by the dispersion losing all color and being completely transparent. Again, the valve between the second and third vessels was slowly opened with the syringe pump set to maintain a constant pressure in the first two vessels. Once the remaining liquid was in the third vessel, the system was depressurized. The remaining liquid in the third vessel was collected out the valve at the bottom of the apparatus. The

system was then disassembled and each vessel was washed with hexane to recollect precipitated particles.

From these experiments, a successful separation was very evident. The system was effectively separating a very polydisperse original dispersion into two less polydisperse fractions. However, the system was also washing a significant portion of the particles into the next vessel. This was due to a vapor block occurring between vessels. As the valve was opened and dispersion flow began, CO_2 left the liquid phase to equilibrate pressure between the two vessels. Eventually, the pressures above and below the dispersion were equal and a vapor block occurred preventing any further flow. At this point, CO_2 would need to be vented from the lower vessel, which would drop the pressure in the higher vessel as well and redisperse a portion of the precipitated particles. This would then require several cycles to push the dispersion through to the lower vessel and would, inadvertently, wash some practices through to the lower vessel. To remedy this, side-ports were tapped into the side of the vessels to allow pressure to equilibrate throughout the system and allow for only gravity induced flow between the vessels.

Similar experiments were, again, performed and the wash through was no longer occurring. From TEM analysis of the recovered fractions, the largest particles were precipitating out as expected, however, some of the smaller particles were still being collected in the first two fractions (which shouldn't occur). This was due to a small amount of liquid being entrained in the higher vessels. At the bottom of each vessel is a flat fitting to reduced the ¾'' opening to a ½'' tubing fitting. The flatness of the fitting was trapping some of the liquid containing smaller particles in the vessels with larger particles. To remedy this, the fittings were machined to have a conical shape (as shown in Figure 24) to prevent entrainment.

At this point, all apparatus modifications were complete and successful, effective separations were being performed. The goal of the experiments then changed from investigating the effectiveness of the apparatus, to examining how effective the technique was at larger scales. Larger volumes of dispersions were used, on the order of 20 mL of a 1 mg / mL silver, dodecanethiol capped nanoparticle in hexane dispersion. Also, rather than just obtaining two fractions, we could now obtain three fractions. The first fraction would contain the largest particles and any misshapen particles, the second fraction would be the narrowest (most monodisperse) fraction, and the third fraction would contain the smallest particles. In order to compare the scale-up apparatus to the spiral tube apparatus, pressures of 600and 650 were selected to give fractions similar to those with the spiral tube. With the apparatus being significantly different, the experiments followed a slightly different course. With the equilibrium pressure lines being run to each vessel, simultaneously, all three vessels were pressurized and held at constant pressures. Along with standard separations of a very polydisperse original sample, the second fraction was saved and recursively fractioned several times to investigate the effectiveness of recursive fractions which were shown to be very effective in the smaller spiral tube apparatus.

A summary of results of these experiments can be seen in Table 10 and Figure 25. Starting with an original sample with average diameter 5.59 nm and 50.7% relative standard deviation, after separation, three fractions with average diameters (and relative standard deviations) of 7.00 nm (41%), 4.35 (21.7%), and 3.95 (27.7%) for the fractions collects at 625 PSI, 650 PSI, and the remaining liquid, respectively). While the separation isn't as effect as the spiral tube, we have shown that it is very effective at separating a very polydisperse original dispersion. Recursive fractionations were shown to improve the monodispersity only slightly, where with the spiral tube, recursive fractionations showed drastic improvements. This is believed to be due to very dilute fractions were used in the recursive fractionations. With dilute solutions, the particles are so far apart from each other in solution, weakening the solvent isn't enough to force the van der Waals forces to induce precipitation. We have found that when the fractions are concentrated, recursive fractionations are more effective.

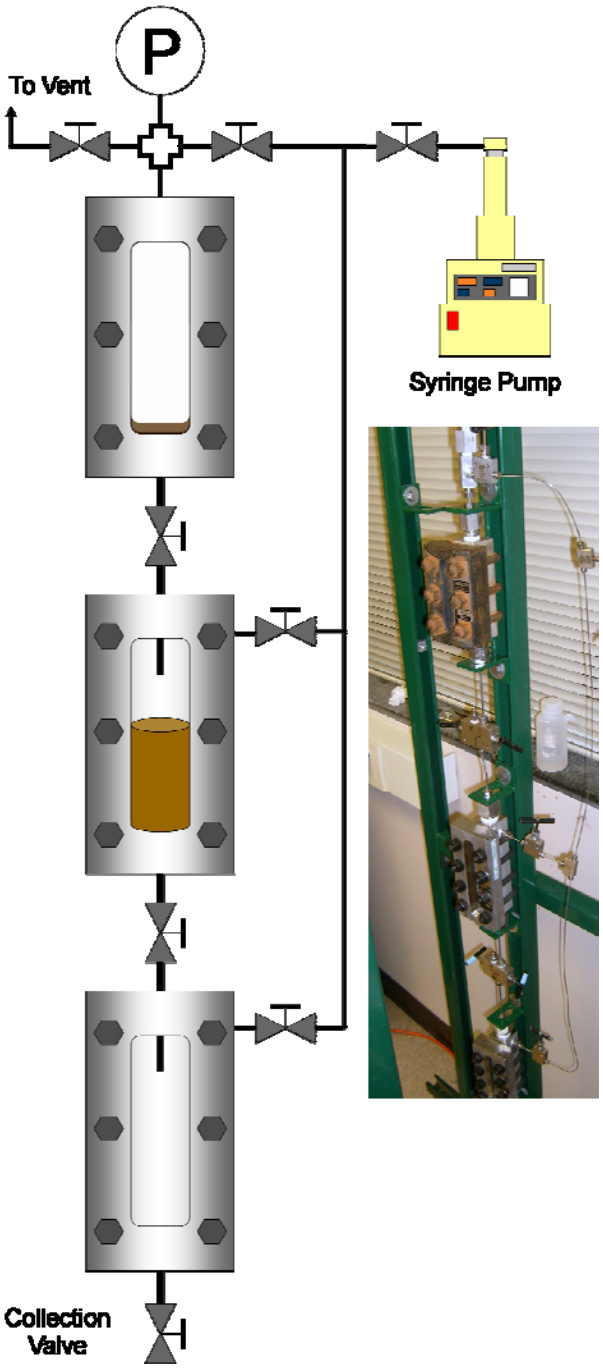

Figure 23 - Schematic of Scale-Up Apparatus

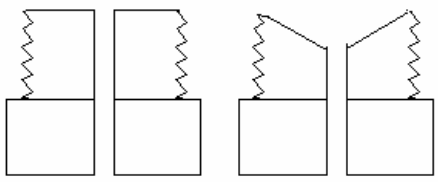

Figure 24 - Modification of Stock Fittings to Prevent Entrainment

Table 10 - Summary of Separation Results

		Scaled-Up Apparatus				Spiral Tube Apparatus		
Fraction Name	Pressure Range (psi)	Ave. Diameter (nm)	Std. Dev. (nm)	Rel. Std. Dev. (%)	% Mass Recovered*	Ave. Diameter (nm)	Std. Dev. (nm)	Rel. Std. Dev.
Original Dispersion	N/A	5.59	2.83	50.7%	N/A	5.0	1.3	26.0%
Fraction 1	0 - 625	7.00	2.87	41.0%	78.1%	N/A	N/A	N/A
Fraction 2	625 - 650	4.35	0.95	21.7%	11.9%	5.0	0.5	11.0%
Fraction 3	650 - 700	3.95	1.10	27.7%	2.7%	3.4	0.7	20.6%
Recursive 1	625 - 650	4.35	0.95	21.7%	11.9%	5.0	0.7	13.1%
Recursive 2	625 - 650	4.50	0.89	19.8%	28.8%	5.0	0.5	10.0%
Recursive 3	625 - 650	4.58	0.83	18.1%	33.5%	4.9	0.4	8.1%

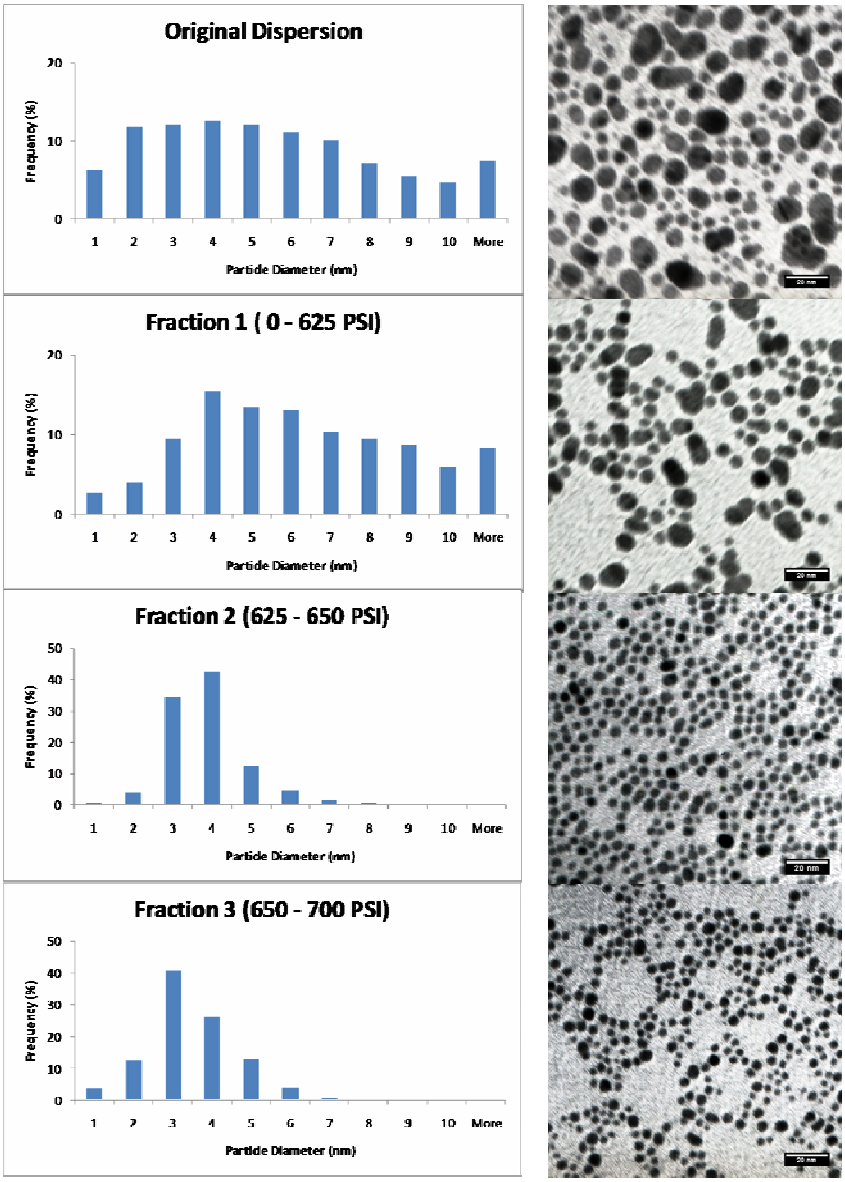

Figure 25 - Size Distributions and TEM Micrographs

Conclusions

We have shown the development of method and the apparatus for precise, rapid, pressure tunable, size selective nanoparticle precipitation and redispersion using tunable CO_2 gas-expanded liquids. This technique has shown to be a marked improvement over the current techniques of nanoparticle fractionation employing liquid antisolvent techniques. As such, there is great promise for this technique to allow us to address the remaining specific aims of this project including larger scale separation of nanoparticles. In this size separation process, dodecanethiol stabilized polydisperse silver and gold nanoparticles dispersed in hexane were fractionated into monodisperse fractions using CO_2 pressurization in the range of 500-700psi. The original sample of dodecanethiol stabilized gold particles of 26% polydispersity were successfully separated into fractions of as little as 11% polydispersity in a single step process. The effect of various parameters on the size separation process was studied. We have concluded that variations in solvent length from five to eight hydrocarbon chains have a significant effect on the pressures required for precipitation of dodecanethiol coated gold nanoparticles. Experiments in which the thiol stabilizing ligand length was varied illustrated that dodecanethiol provides the strongest solvent - ligand tail interaction when hexane was the bulk solvent medium. We have found that this new process is very fast, repeatable and reproducible requiring very short holding time at each precipitation stage. It was found that as the solvent temperature was increased an increase in CO_2 pressure is required to completely precipitate all the nanocrystals from solution. Recursive fractionations on a sample collected within a given pressure range elicit the desired nanoparticles of a precise size. The effect of time on the size separation process shows that this new process is very fast, repeatable and reproducible requiring very short holding time at each precipitation stage.

We have also demonstrated that CO_2 can be use as an antisolvent to successfully size separate and fractionate the CdSe/ZnS core shell quantum dots through pressure tunable gas expanded liquids in a single step process. Compared to traditional liquid anti-solvent technique, this is a rapid, precise, pressure tunable and green size precipitation technique. This has certainly proven to be a useful tool for applications of metal nanocrystals and quantum dots where similar sized nanoparticles are required.

A model was developed on the basis of total interaction energy to predict the threshold Ag nanoparticle size which can be precipitated/dispersed in CO_2 gas expanded liquids at various antisolvent CO_2 pressures. After deriving expressions for the osmotic energy term and the Hamaker constant that account for multiple solvent systems, the model was successfully applied to the CO_2 gas expanded liquid size separation process using the thermodynamic properties of CO_2 gas expanded liquids. However, allowing complete solvation of the ligand length in the model results in threshold particle sizes too large compared to the experimental results. Thus, three phenomenological variations of this total interaction energy model were considered where the Limited Ligand Length Solvation Model provided the best match of the threshold predicated particle sizes with the experimental results. This model shows that the degree of tail solvation strongly impacts the particle sizes and that limited ligand solvation is occurring and is a function of CO_2 pressure. Very subtle changes in solvent strength result in a fine tuning of dispersed particle size and this modeling study improves our understanding of particle dispersibility at various conditions alleviating the need for extensive experimentation.

Furthermore, we have shown that this CO_2-expanded liquid separation process can be successfully scaled up to effectively fractionate ligand stabilized nanoparticle dispersions of more than 20 ml.

References:

(1) Anand, M.; McLeod, M. C.; Bell, P. W.; Roberts, C. B. Journal of Physical Chemistry B 2005, 109, 22852.
(2) Arnaud, I.; Abid, J.-P.; Roussel, C.; Girault, H. H. Chemical Communications (Cambridge, United Kingdom) 2005, 787.
(3) McLeod, M. C.; Anand, M.; Kitchens, C. L.; Roberts, C. B. Nano Letters 2005, 5, 461.
(4) Brust, M.; Walker, M.; Bethell, D.; Schiffrin, D. J.; Whyman, R. Journal of the Chemical Society, Chemical Communications 1994, 801.
(5) Peng, D.-Y.; Robinson, D. B. Industrial & Engineering Chemistry Fundamentals 1976, 15, 59.
(6) Creighton, J. A.; Eadon, D. G. Journal of the Chemical Society, Faraday Transactions 1991, 87, 3881.
(7) Prasad, B. L. V.; Stoeva, S. I.; Sorensen, C. M.; Klabunde, K. J. Langmuir 2002, 18, 7515.
(8) Korgel, B. A.; Fullam, S.; Connolly, S.; Fitzmaurice, D. Journal of Physical Chemistry B 1998, 102, 8379.
(9) Kitchens, C. L.; McLeod, M. C.; Roberts, C. B. Journal of Physical Chemistry B 2003, 107, 11331.
(10) Shah, P. S.; Holmes, J. D.; Johnston, K. P.; Korgel, B. A. Journal of Physical Chemistry B 2002, 106, 2545.
(11) McLeod, M. C.; Kitchens, C. L.; Roberts, C. B. Langmuir 2005, 21, 2414.
(12) Sigman, M. B., Jr.; Saunders, A. E.; Korgel, B. A. Langmuir 2004, 20, 978.
(13) Lee, C. T., Jr.; Johnston, K. P.; Dai, H. J.; Cochran, H. D.; Melnichenko, Y. B.; Wignall, G. D. Journal of Physical Chemistry B 2001, 105, 3540.
(14) Martin, J. E.; Wilcoxon, J. P.; Odinek, J.; Provencio, P. Journal of Physical Chemistry B 2000, 104, 9475.
(15) Eckert, C.A.; Bush, D.; Brown, J.S.; Liotta, C.L. Industrial & Engineering Chemistry Research, 39, 4615, 2000.
(16) Jessop, P.G.; Subramaniam, B. Chemical Reviews, 107, 2666, 2007.
(17) McLeod, M.C.; Kitchens, C.L.; Roberts, C.B. Langmuir, 21, 2414, 2005.
(18) Liu, J.; Anand, M.; Roberts, C.B. Langmuir, 22, 3964, 2006.
(19) Zhang, J.; Han, B.; Liu, J.; Zhang, X.; Liu, Z.; He, J. Chemical Communications, 2724, 2001.
(20) Anand, M.; McLeod, M.C.; Bell, P.W., Roberts, C.B. Journal of Physical Chemistry B, 109, 22852, 2005.
(21) McLeod, M.C.; Anand, M.; Kitchens, C.L.; Roberts, C.B. Nano Letters, 5, 461, 2005.
(22) Anand, M.; Odom, L.A.; Roberts, C.B. Langmuir; 23, 7338, 2007.
(23) Kitchens, C.L.; McLeod, M.C.; Roberts, C.B. Journal of Physical Chemistry B, 107, 11331, 2003.
(24) Shah, P.S.; Holmes, J.D.; Johnston, K.P.; Korgel, B.A. Journal of Physical Chemistry B, 106, 2545, 2002.
(25) Kitchens, C.L.; Roberts, C.B. Industrial & Engineering Chemistry Research, 43, 6070, 2004.
(26) Shah, P.S.; Husain, S.; Johnston, K.P.; Korgel, B.A. Journal of Physical Chemistry B, 106, 12178, 2002.
(27) Hamaker, H.C. Physica (The Hague), 4, 1058, 1937.
(28) Israelachvili, J.N. Intermolecular and surface forces: with applications to colloidal and biological systems; London, 1985.
(29) Sun, Y.; Shekunov, B.Y.; York, P. Chemical Engineering Communications, 190, 1, 2003.
(30) Lide, D.R. Handbook of Chemistry and Physics, 75th ed., 1994.
(31) Lide, D.R. Handbook of Organic Solvents; CRC: Boca Raton, FL, 1995.
(32) Vincent, B.; Luckham, P.F.; Waite, F.A. Journal of Colloid and Interface Science, 73, 508,

1980.
(33) Saunders, A.E.; Korgel B.A. Journal of Physical Chemistry B, 108, 16732, 2004.
(34) Korgel, B.A.; Fullam, S.; Connolly, S.; Fitzmaurice, D. Journal of Physical Chemistry B, 102, 8379, 1998.
(35) Eichenlaub, S.; Chan, C.; Beaudoin, S.P. Journal of Colloid and Interface Science, 248, 389, 2002.
(36) Brochard, F.; De Gennes, P.G. Macromolecules, 10, 1157, 1977.
(37) De Gennes, P.G. Macromolecules, 9, 594, 1976.
(38) De Gennes, P.G. Macromolecules, 9, 587, 1976.
(39) Porter, M.D.; Bright, T.B.; Allara, D.L.; Chidsey, C.E.D. Journal of the American Chemical Society, 109, 3559, 1987.

PROJECT RELATED PUBLICATIONS

- M. Anand, S.S. You, S. Saunders, K. Hurst, C.L. Kitchens, W.R. Ashurst, C. B. Roberts, "Thermodynamic Analysis of Nanoparticle Size Selective Fractionation Using Gas Expanded Liquids," in press in *Industrial & Engineering Chemistry Research, 2008*.
- Anand, M.; Odom, L. A.; Roberts, C. B. "Finely Controlled Size-Selective Precipitation and Separation of CdSe/ZnS Semiconductor Nanocrystals Using CO2-Gas-Expanded Liquids" Langmuir; 23(13); 7338-7343, 2007.
- Roberts, C.B., Anand, M., Liu, J., "Fractionation of Metal and Semiconductor Nanoparticles and Their Deposition into Wide Area Thin Films and Ordered Arrays Using CO2- Expanded Liquid Solutions, Proceedings of the European Congress of Chemical Engineering – 6, pg. 247-248, 2007.
- Roberts, C.B., "Metal and Semiconductor Nanoparticle Deposition and Size Fractionation Using CO2-Expanded Liquids and Supercritical CO2 processing," Supergreen – The 5th International Symposium on Supercritical Fluids, KL-12, p.8, 2007.
- Dutta, P.; Pal, S.; Seehra, M.S.; Anand, M.; Roberts, C.B. "Magnetism in dodecanethiol-capped gold nanoparticles: Role of size and capping agent" Applied Physics Letters, 90 (21): Art. No. 213102 , 2007.
- M. Anand, P. W. Bell, C. B. Roberts, "Synthesis and Stearic Stabilization of Silver Nanoparticles in Carbon dioxide Using Fluorine-Free Compounds," J. Phys. Chem.B (2006), 110(30), 14693-14701.
- J. Liu, M. Anand, C. B. Roberts, "Synthesis and Extraction of β–D glucose Stabilized Au Nanoparticles Processed into Low Defect, Wide Area Thin Films And Ordered Arrays Using CO2-Expanded Liquids," Langmuir (2006), 22(9), 3964-3971.

PROJECT RELATED PRESENTATIONS

- Roberts, C.B., Anand, M., Liu, J., "Fractionation of Metal and Semiconductor Nanoparticles and Their Deposition into Wide Area Thin Films and Ordered Arrays Using CO2- Expanded Liquid Solutions, European Congress of Chemical Engineering – 6, Copenhagen, Denmark, September 17, 2007.
- Roberts, C.B., "Metal and Semiconductor Nanoparticle Deposition and Size Fractionation Using CO2-Expanded Liquids and Supercritical CO2 processing," Supergreen – The 5th International Symposium on Supercritical Fluids, Seoul, South Korea, November 29, 2007.
- M. Anand, Seong-Sik You, C.L. Kitchens, W. R. Ashurst, and C. B. Roberts, "Fractionation of metal and semiconductor nanoparticles using CO2-expanded liquids: Experiment and theory," I&EC 99, ACS National Meeting, Boston, MA, August 23, 2007.
- M. Anand, Seong-Sik You, K.M. Hurst, S.R. Saunders, C.L. Kitchens, W. R. Ashurst, and C. B. Roberts, "Thermodynamic Analysis of the Gas Expanded Liquid Nanoparticle Size Separation Process," 542b, *AIChE 2007 Annual Meeting, Salt Lake City*, November 8, 2007.
- S.R. Saunders and C. B. Roberts, "Scale-Up Of A Nanoparticle Size-Selective Fractionation Process Using CO_2-Expanded Liquids," *328l, AIChE 2007 Annual Meeting, Salt Lake City*, November 6, 2007.
- C. B. Roberts, "Metal and Semiconductor Nanoparticle Deposition and Separation using CO2-Expanded Liquids and Supercritical CO2 Processing," Invited Seminar, Tulane University, Department of Chemical Engineering, April 27, 2007.
- Anand, M., Odom, L., Roberts, C. B., "Separation of Polydisperse Metal and Semiconductor Nanoparticle Populations into Monodisperse Fractions using CO_2 Expanded Liquids," to be presented at *AIChE 2006 Annual Meeting, San Francisco* , November12-17, 2006
- Anand, M**.**, Bell, P. W., Roberts, C. B., "Synthesis and Steric Stabilization of Silver Nanoparticles in Neat Carbon Dioxide Solvent Using Fluorine-Free Compounds," to be presented at *AIChE 2006 Annual Meeting, San Francisco*, November 12-17, 2006
- Anand, M., Bell, P. W., Roberts, C. B., "Benign process for Silver nanoparticles synthesis and processing in neat Carbon dioxide solvent using Fluorine-free compounds," *10th Annual Green Chemistry and Engineering Conference*, Washington, DC, June 26-30, 2006

- Liu, J., Anand, M., Roberts, C. B., "Synthesis and Extraction of β–D glucose Stabilized Au Nanoparticles Processed into Low Defect, Wide Area Thin Films And Ordered Arrays Using CO_2-Expanded Liquids," *10th Annual Green Chemistry and Engineering Conference*, Washington, DC, June 26-30, 2006
- Roberts, C.B., Anand, M., Liu, J., Bell, P.W., "Metallic nanoparticle deposition and separation using CO_2-expanded liquids and supercritical CO_2 processing", *Invited seminar,* Georgia Institute of Technology, Department of Chemical Engineering, April 5, 2006.
- Roberts, C.B., Anand, M., Liu, J., "Metallic nanoparticle deposition and separation using CO_2-expanded liquids and supercritical CO_2 processing", *Invited seminar*, Tennessee Technical University, Department of Chemical Engineering, March 30, 2006.

Appendix A

This Appendix provides the derivations of the Hamaker constant and the osmotic repulsive energy term for a mixture of solvents and one polymer (i.e. ligand tails). The procedure and calculations for estimating ligand surface coverage is also presented.

Derivation of Hamaker constant for mixed solvent interacting with one polymer component.

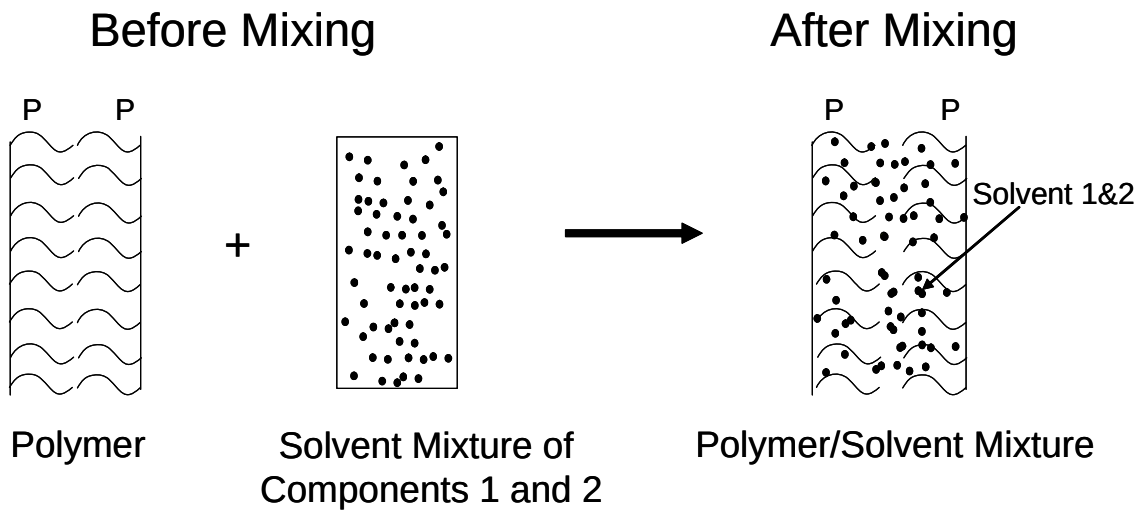

The summation of the component interactions before mixing of the polymer (P) with the solvent mixture of components 1 and 2 is given by Equation A1

$$k(P - P) + \alpha(1-1) + \beta(2-2) + \gamma(1-2) + \gamma(2-1) \quad \text{(A1)}$$

where k, α, β, and γ denote coefficients of interaction for dispersion forces. Since random mixing has been assumed, the coefficients α, β, and γ are proportional to the product of the volume fractions of the species involved. This means that the contact probability of (1-1) would be $\tilde{\phi}_1^2$, the contact probability of (1-2) would be $\tilde{\phi}_1 \tilde{\phi}_2$ and the contact probability of (2-2) would be $\tilde{\phi}_2^2$, where $\tilde{\phi}_1$ and $\tilde{\phi}_2$ represent the volume fractions of the solvent components 1 and 2 excluding the polymer. Combining $\alpha = k\tilde{\phi}_1^2$, $\beta = k\tilde{\phi}_2^2$, $\gamma = k\tilde{\phi}_1 \tilde{\phi}_2$ and Equation A1 becomes

$$k\left\{(P - P) + \tilde{\phi}_1^2(1-1) + \tilde{\phi}_2^2(2-2) + 2\tilde{\phi}_1 \tilde{\phi}_2 (1-2)\right\} \quad \text{(A2)}$$

Taking the basis as two polymer chains, the proportionality constant, k,is equal to 1, such that Equation A2 becomes:

$$(\mathrm{P}\text{-}\mathrm{P}) + \tilde{\phi}_1^{\,2}(1-1) + \tilde{\phi}_2^{\,2}(2-2) + 2\tilde{\phi}_1\,\tilde{\phi}_2\,(1-2) \tag{A3}$$

After mixing the polymer (P) with the solvent mixture of components 1 and 2, the summation of the component interactions is given by Equation A4

$$2x(\mathrm{P}-1) + 2y(\mathrm{P}-2) \tag{A4}$$

where *x* and *y* are unknown coefficients of contact probabilities, with *x* and *y* summing to 1. Applying a component balance for solvent 1 before and after mixing using Equations A3 and A4 yields

$$2\tilde{\phi}_1^{\,2} + 2\tilde{\phi}_1\,\tilde{\phi}_2 = 2x \tag{A5}$$

and since the volume fractions sum to 1, simplifying results in

$$\tilde{\phi}_1 = x \tag{A6}$$

Similarly, applying the component balance on solvent 2 will result in $\tilde{\phi}_2 = y$.

Now, the expression for the Hamaker constant for a mixed solvent-polymer interaction, A_{PMP}, can be derived by subtracting the Hamaker constants of component interactions of Equation A3 from the Hamaker constants of component interactions of Equation A4, yielding Equation A7 where *P* denotes the polymer and *M* denotes the mixed solvent.

$$\mathrm{A_{PMP}} = -\left[\mathrm{A_{PP}} + \tilde{\phi}_1^{\,2}\mathrm{A_{11}} + 2\tilde{\phi}_1\tilde{\phi}_2\mathrm{A_{12}} + \tilde{\phi}_2^{\,2}\mathrm{A_{22}} - 2\tilde{\phi}_1\mathrm{A_{P1}} - 2\tilde{\phi}_2\mathrm{A_{P2}}\right]$$

$$\mathrm{A_{PMP}} = -\left[\mathrm{A_{PP}} - 2\tilde{\phi}_1\mathrm{A_{P1}} - 2\tilde{\phi}_2\mathrm{A_{P2}} + \left(\tilde{\phi}_1\sqrt{\mathrm{A_{11}}} + \tilde{\phi}_2\sqrt{\mathrm{A_{22}}}\right)^2\right]$$

assuming

$$\mathrm{A_{12}} = \sqrt{\mathrm{A_{11}}}\sqrt{\mathrm{A_{22}}}$$

yields

$$\mathrm{A_{PMP}} = -\left[\sqrt{\mathrm{A_{PP}}} - \left(\tilde{\phi}_1\sqrt{\mathrm{A_{11}}} + \tilde{\phi}_2\sqrt{\mathrm{A_{22}}}\right)\right]^2 \tag{A7}$$

The expression for the Hamaker constant can be obtained for a mixed solvent-polymer interaction. Since the negative sign is already taken into account in the van der Waals attractive potential term in the total interaction energy, the negative sign in front of Hamaker constant can be neglected. Therefore, the combined Hamaker constant, A_{PMP}, is given as

$$A_{PMP} = \left[\sqrt{A_{PP}} - \left(\tilde{\phi}_1\sqrt{A_{11}} + \tilde{\phi}_2\sqrt{A_{22}}\right)\right]^2 \quad \text{(A8)}$$

Derivation of the osmotic repulsion term for mixed solvent interacting with one polymer in the volume fraction model.

The Gibbs free energy change for mixing, $\Delta G_{M,}$ in a volume element, δV, is given by Equation A9:

$$\delta(\Delta G_M) = \delta(\Delta G^C) + \delta(\Delta G^R) \quad \text{(A9)}$$

where ΔG^C is the combinatorial free energy and ΔG^R is the residual free energy. For the combinatorial free energy, which is purely entropic in nature, it is assumed that the polymer amount can be neglected in the bulk solvent system due to a very low concentration compared to that of the solvent. The combinatorial free energy can be expressed as the following.

$$\delta(\Delta G^C) = k_B T \sum \delta n_i \ell n \phi_i \cong k_B T \sum_j^s \delta n_j \ell n \phi_j \quad \text{(A10)}$$

where i represents component i in the system, j represents components j in the solvent mixture excluding the polymer, and s is the number of solvent components.

The volume fraction, ϕ_j of component j in the system is given by

$$\phi_j = \tilde{\phi}_j(1 - \phi_p) \quad \text{(A11)}$$

where $\widetilde{\phi}_j$ is a volume fraction of component *j* excluding polymer, ϕ_p is a volume fraction of polymer *p* in the entire solvent-polymer system. The number of molecules, δn_j of component *j* in the system is given by

$$\delta n_j = \frac{x_j(1-\phi_p)\delta \mathrm{V}}{v_M} \tag{A12}$$

where x_j is the mole fraction of component *j* in the solvent mixture and v_M represents the molar volume of the solvent mixture excluding the polymer ($v_M = \sum x_j v_j$ where v_j is molar volume of component *j* in solvent mixture excluding polymer) and *V* is the total volume of the system. Substituting Equations A11 and A12 into Equation A10, and using the expression for the logarithmic term in the Taylor series expansion at the limit of ϕ_p approaching zero, yields the following expression for the combinatorial Gibbs free energy:

$$\delta\left(\Delta \mathrm{G}^{\mathrm{C}}\right) = k_B T \sum_j^s x_j \left(\ln\widetilde{\phi}_j - \phi_p - \frac{{\phi_p}^2}{2} \right)\left(\frac{1-\phi_p}{v_M} \right)\delta V \tag{A13}$$

The residual free energy, which is the free energy arising from contact dissimilarities, is given by the following expression:

$$\delta\left(\Delta \mathrm{G}^{\mathrm{R}}\right) = k_B T \sum_{j<}^s \sum_k^s \chi_{jk}\delta\left(r_j n_j\right)\phi_k \tag{A14}$$

where r_j is the segment length of the molecule *j*, ϕ_k is a volume fraction of component k, n_j is number of molecules and χ_{jk} is the Flory-Huggins interaction parameter. The residual free energy is the sum of the excess free energies associated with the interaction of solvent component *j* to the other solvent component *k* with volume fraction ϕ_k and polymer component *p* with volume fraction ϕ_p.

After substituting Equation A12 into Equation A14, the following expression is obtained:

$$\delta\left(\Delta \mathrm{G}^{\mathrm{R}}\right)=k_{B}T\left[\sum_{j}^{s}\sum_{k>j}^{s}\chi_{jk}r_{j}x_{j}\phi_{k}+\sum_{j}^{k}\chi_{jp}r_{j}x_{j}\phi_{p}\right]\left(\frac{1-\phi_{p}}{v_{M}}\right)\delta V \tag{A15}$$

Substituting Equation A11 for ϕ_k in yields the following expression for the residual Gibbs free energy:

$$\delta\left(\Delta \mathrm{G}^{\mathrm{R}}\right)=k_{B}T\left[\sum_{j}^{s}\sum_{k>j}^{s}\chi_{jk}r_{j}x_{j}\widetilde{\phi}_{k}\left(1-\phi_{p}\right)+\sum_{j}^{k}\chi_{jp}r_{j}x_{j}\phi_{p}\right]\left(\frac{1-\phi_{p}}{v_{M}}\right)\delta V \tag{A16}$$

Repulsive potential energy terms.

According to Napper (Napper, D. H. *Polymeric Stabilization of Colloidal Dispersions*, 1983), it is assumed that the free energy of attachment of the polymer chains is independent of the separation distance, *d*, of the plates, and the repulsive potential energy, ΔG_R, is

$$\Delta \mathrm{G}_{R}=\Delta \mathrm{G}_{M_{d}}-\Delta \mathrm{G}_{M_{\infty}} \tag{A17}$$

Assuming that $\{\mathrm{x_j}\}$ and $\{\widetilde{\phi}_k\}$ are independent of the distance of the separation, substituting $\phi_p=v_s\rho_p(d)$ into Equations A13 and A16 yields

$$\Delta \mathrm{G}_{\mathrm{R}}=k_{B}T\left[\sum_{j}^{s}x_{j}\left(\frac{1}{2}+r_{j}\sum_{k>j}\widetilde{\phi}_{k}\chi_{jk}-r_{j}\chi_{jp}\right)\right]\frac{{v_{s}}^{2}}{v_{M}}\left[\int_{V}{\rho_{p}}^{2}(d)\,dV-\int_{V}{\rho_{p}}^{2}(\infty)\,dV\right] \tag{A18}$$

where, $\rho_p(d)$ is the number density of the polymer and v_s is the segment volume of the molecule. As in Napper's derivation for a binary system, all terms except ${\rho_p}^2(d)$ terms vanish.

Assuming constant segment density and that the particles are equivalent spheres, we can obtain the expression of the osmotic interaction energy by applying the Derjaguin approximation.

$$\Phi_{\mathrm{osm}}=\frac{4\pi Rk_{\mathrm{B}}T}{(v_{M}/N_{av})}\phi^{2}\left[\sum_{j}^{s}x_{j}\left(\frac{1}{2}+r_{j}\sum_{k>j}\widetilde{\phi}_{k}\chi_{jk}-r_{j}\chi_{jp}\right)\right]\left(l-\frac{h}{2}\right)^{2} \qquad \text{for } l<h<2l \tag{A19}$$

$$\Phi_{\mathrm{osm}}=\frac{4\pi Rk_{\mathrm{B}}T}{(v_{M}/N_{av})}\phi^{2}\left[\sum_{j}^{s}x_{j}\left(\frac{1}{2}+r_{j}\sum_{k>j}\widetilde{\phi}_{k}\chi_{jk}-r_{j}\chi_{jp}\right)\right]\left[l^{2}\left(\frac{h}{2l}-\frac{1}{4}-\ln\left(\frac{h}{l}\right)\right)\right] \qquad \text{for } h<l \tag{A20}$$

$$h=d-2R$$

Derivation of the osmotic repulsion term for mixed solvent interacting with one polymer in the surface fraction model

In the surface fraction model, the Gibbs free energy change for mixing is again given by Equation A9 where $\delta(\Delta G^C)$ is the same as in Equation A13 and $\delta(\Delta G^R)$ is given by:

$$\delta(\Delta G^R) = k_B T \sum_j^s \sum_{k>j}^s \Delta\varepsilon_{jk} \delta(q_i n_i)\theta_k \tag{A21}$$

where $\Delta\varepsilon_{jk}$ is the interaction parameter analogous to the Flory- Huggins parameter (χ_{jk}), q_i is the surface area of component i, θ_i is the surface fraction of component i, and n_i is the number of molecules of component i. Therefore, fraction θ_k is given by

$$\theta_k = \frac{q_k n_k}{\sum_i^n q_j n_j} = \frac{s_k \phi_k}{S_M} \tag{A22}$$

where

$$S_M = \sum_i^n s_j \phi_j$$

$$s_k = \frac{q_k}{r_k}$$

$$\phi_k = \frac{r_k n_k}{\sum_j^n r_j n_j}$$

In Equation A22, r_j is the segment number of component j, s_j is the ratio of surface area and segment number of component j.

The Taylor series expansion of θ_k and θ_p at the limit of ϕ_p approaching zero yields

$$\theta_k = \frac{s_k \bar{\phi}_k}{\bar{S}_M} - \frac{s_k s_p \bar{\phi}_k}{\bar{S}_M{}^2} \phi_p + \frac{s_k s_p \bar{\phi}_k (s_p - \bar{S}_M)}{\bar{S}_M{}^3} \phi_p \tag{A23}$$

$$\theta_p = \frac{s_p}{\bar{S}_M} \phi_p + \frac{s_p (\bar{S}_M - s_p)}{\bar{S}_M{}^2} \phi_p{}^2 \tag{A24}$$

As in Equation A17, the repulsive potential energy, ΔG^R, given by

$$\Delta G_R = \Delta G_d - \Delta G_\infty \tag{A25}$$

Substituting the above expressions in an analogous manner to that of the development of Equation A18, the following expression for the repulsive potential energy for the surface fraction model is given by

$$\Delta G_R = k_B T \frac{s_p^{\,2}}{\bar{S}_M^{\,2}} \left[\frac{1}{2} + \sum_j^s r_j s_j x_j \left[\sum_j^s s_k \bar{\phi}_k \frac{\Delta\varepsilon_{jk}}{\bar{S}_M} - \Delta\varepsilon_{jp} \right] \right] \frac{v_s^{\,2}}{\bar{v}_{solv}} \left[\int_V \rho_p^{\,2}(d)\, dV - \int_V \rho_p^{\,2}(\infty)\, dV \right] \tag{A26}$$

Assuming constant segment density and that the particles are equivalent spheres, we can obtain the expression of the osmotic interaction energy by applying the Derjaguin approximation.

$$\Phi_{osm} = \frac{4\pi R k_B T}{(v_M / N_{av})} \phi^2 \frac{s_p^{\,2}}{\bar{S}_M^{\,2}} \left[\frac{1}{2} + \sum_j^s r_j s_j x_j \left[\sum_{k>j}^s s_k \tilde{\phi}_k \frac{\Delta\varepsilon_{jk}}{\bar{S}_M} - \Delta\varepsilon_{jp} \right] \right] \left(l - \frac{h}{2} \right)^2 \qquad \text{for } l < h < 2l \tag{A27}$$

$$\Phi_{osm} = \frac{4\pi R k_B T}{(v_M / N_{av})} \phi^2 \frac{s_p^{\,2}}{\bar{S}_M^{\,2}} \left[\frac{1}{2} + \sum_j^s r_j s_j x_j \left[\sum_{k>j}^s s_k \tilde{\phi}_k \frac{\Delta\varepsilon_{jk}}{\bar{S}_M} - \Delta\varepsilon_{jp} \right] \right] \left[l^2 \left(\frac{h}{2l} - \frac{1}{4} - \ln\left(\frac{h}{l} \right) \right) \right] \qquad \text{for } h < l \tag{A28}$$